An investigation into the feasibility of applying 3D geological modeling techniques to polar ice sheets

Bachelor's Thesis

Submission Date: March 27th, 2015

at

Fachbereich Geowissenschaften

Eberhard Karls Universität

Tübingen

and

Alfred Wegener Institut

Helmholtz-Zentrum für Polar- und Meeresforschung

Bremerhaven

Name: Felicitas Mundel

1st Supervisor: Prof. Dr. Paul Bons

2nd Supervisor: Dr. Daniela Jansen

Declaration of Authorship

I hereby declare that I have written this thesis entirely on my own and without others than the acknowledged sources. All passages and phrases which are literally or in general taken from books, publications or other sources are marked as such.

This thesis was neither as a whole nor in essential parts subject of another examination procedure.

Tübingen, March 27th, 2015

_____

Felicitas Mundel

Abstract

Due to their important role for understanding the previous and further development of earth's climate, the structure and processes of polar ice sheets are subjects of high scientific interest. For the first time, a 3D model of internal ice layers of the Greenland Ice Sheet is proposed. It was created with the structural geologic software MOVE, using Radar Depth Sounder profiles of the catchment of Petermann Glacier, located in North-West Greenland. The model visualizes the large-scale folding of the ice layers and shows that basic geologic processes are mainly responsible for the creation of these cylindrical folds: The funnel-shaped channel of Petermann Glacier leads to compression across flow direction, while increasing ice velocity causes local tensile stress along flow. In deep ice layers, sheath folds are present. Due to decreasing ice velocity towards the bottom of the ice column, a strong shear stress acts on the ice layers, which leads to the formation of sheath folds.

Zusammenfassung

Aufgrund ihrer wichtigen Rolle zum Verständnis der bisherigen und zukünftigen Entwicklung des Klimas der Erde sind die Struktur und Prozesse der polaren Eisschilde von großem wissenschaftlichem Interesse. Zum ersten Mal wird ein 3D Modell der internen Eisschichten des Grönländischen Eisschildes vorgestellt. Es wurde mit der strukturgeologischen Software MOVE erstellt, unter Verwendung von Radar-Profilen aus dem Einzugsbereich des Petermann-Gletschers, der sich im Nordwesten Grönlands befindet. Das Modell macht die großräumige Faltung der Eisschichten sichtbar und zeigt, dass grundlegende geologische Prozesse hauptverantwortlich für die Bildung dieser zylindrischen Falten sind: Der trichterförmige Kanal des Petermann-Gletschers führt zu Kompression quer zur Fließrichtung, während entlang des Fließens zunehmende Eisgeschwindigkeiten für lokale Dehnungsbeanspruchung sorgen. In tiefen Eisschichten sind sogenannte Futteralfalten (engl. *sheath folds)* vorhanden. Aufgrund abnehmender Eisgeschwindigkeiten nach unten in der Eissäule wirkt eine starke Scherspannung auf die Eisschichten, was zur Entstehung von Futteralfalten führt.

Acknowledgments

I would like to express my gratitude to Paul Bons for fantastic guidance and help throughout my project, for the opportunity to investigate such an interesting topic and for providing me with any material I needed. I also want to thank Daniela Jansen and (my secret third supervisor) Ilka Weikusat for their friendly and patient assistance and for the great possibility to gain insight into the AWI. Many thanks to all three of you for being always reachable for any questions I had! Next, I want to thank all members of the structural geology working group in Tübingen for the great working atmosphere! Special thanks to Tamara de Riese for helpful comments and providing me with literature, to Lutz Eberle and Zhongbao Zhao for assisting me in MOVE, and to Florian Steinbach for supporting discussions and for being good company in Bremerhaven.

My very deep gratitude belongs to my parents, who encourage and support me all my life! And special thanks also to all my friends for being there for me, not only during my *Gletschelorarbeit*.

List of Contents

List of Figures

List of Tables

1 Introduction

In times of global warming and diminishing polar ice sheets, it is very important to understand the processes and dynamics forming such glacial structures to gather further knowledge that can later be used for climate research. In the 1990s and 2000s, the Greenland ice sheet experienced heavy mass loss due to rising temperatures (Rignot et al, 2008). In order to get a better idea of the polar ice sheets, the *Center for Remote Sensing of Ice Sheets* (CReSIS) has been collecting radar data of the ice sheets of Greenland, Canada and Antarctica since 1993 (Gogineni, 2012). In the images derived from these data, large fold-like structures and heavily deformed internal ice layers can be observed (Figure 1 & NEEM community members, 2013).
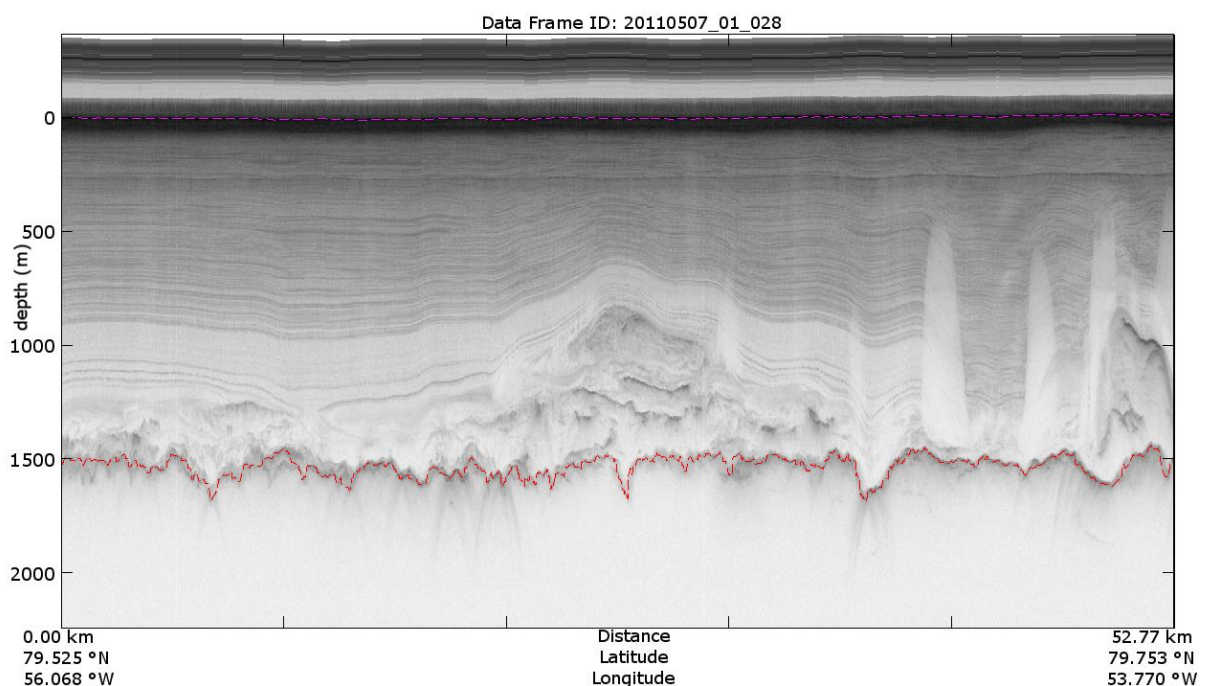
Figure 1. CReSIS' Radar Depth Sounder image, illustrating that deformed internal ice layers occur in polar ice sheets, Petermann Glacier, Greenland. CReSIS file no. 20110507_01_028. Red line shows the position of the bedrock, pink line shows the position of the ice surface. The image is exaggerated by factor ten. (Taken and edited from Gogineni, 2012.)

Some work has already been done to identify the responsible processes that lead to such folds in polar ice sheets. Robin Bell et al. (2014) elaborate that refreezing melt water underneath an ice sheet can lead to deformation of the ice layers and also to warming of the ice, which leads to an increase of the ice velocity close to the grounding line of a glacier. Michael Wolovick et al. (2014) use a thermomechanical ice sheet model to show that slippery patches caused by basal melting travel downstream and can cause significant fold-shaped uplift and subsidence in ice sheets, similar to those observable in the radar images.

NEEM community members (2013) also discuss these disturbed ice layers, stating that the different ice rheology of Eemian and glacial ice might be responsible for the fold structures. They follow the idea that Eemian (interglacial) ice is more rigid and the overlying (glacial) ice got deformed over it, creating said fold-like structures.

Until now, little attention has been paid to the geological processes which are at work in ice, and whether rather primary processes might play a major role in creating the folds. In geology, ice is not regarded as a fluid, but as rock which is close to its melting point. Recently, MacGregor et al. (2015) mention "eye"-like structures in the radar images of the Greenland ice sheet. They resemble the sections of sheath folds occurring in rocks.

However, all these examinations conducted in order to explain the deformations in polar ice sheets did rely on 2D radar images only. No model depicting the three-dimensional structures of the ice sheets has been created yet. This thesis deals with the question whether or not the software MOVE provides the possibility to create a suitable 3D model using the radar imagery provided by CReSIS. In addition, it presents a 3D visualization of internal ice layers in the catchment of Petermann Glacier, Greenland.

Furthermore, this thesis also surveys the possibility that primary processes as the ones occurring in ductile shear zones, where folds are quite common (Hudleston and Treagus, 2010), are involved in the creation of folds in ice sheets. The presented 3D model gives the opportunity to take a closer look to the existing fold-like structures within the Petermann ice sheet layers. Special attention is also paid to the question whether "eye"-shaped patterns in the radar pictures imply that sheath folds are present within the ice sheet.

2   Setting

The study area lies in the north-west of Greenland, the world's largest island. Around 80 % of Greenland is covered by an ice sheet, which extends over an area of approximately 1.7 million square kilometers and spreads between 60° and 84° northern latitude (Hvidberg et al., 2013). The ice sheet has an average thickness of around 1,600 m and a volume of about 3 million cubic kilometers – if the ice sheet melted completely, the sea level would rise about 7 m (Thomas, 2001). The maximal thickness of the ice sheet amounts about 3.3 kilometers (Morlighem et al., 2014).

For this thesis, the catchment area of Petermann Glacier (and partly of Humboldt Glacier) has been chosen (Figure 2a). Located in north western Greenland, the catchments of Petermann and Humboldt Glacier cover an area of approximately 121,000 square kilometers (Rignot and Kanagaratnam, 2006). The center of the study area lies at approximately 79.7° northern latitude and 53.5° western longitude.
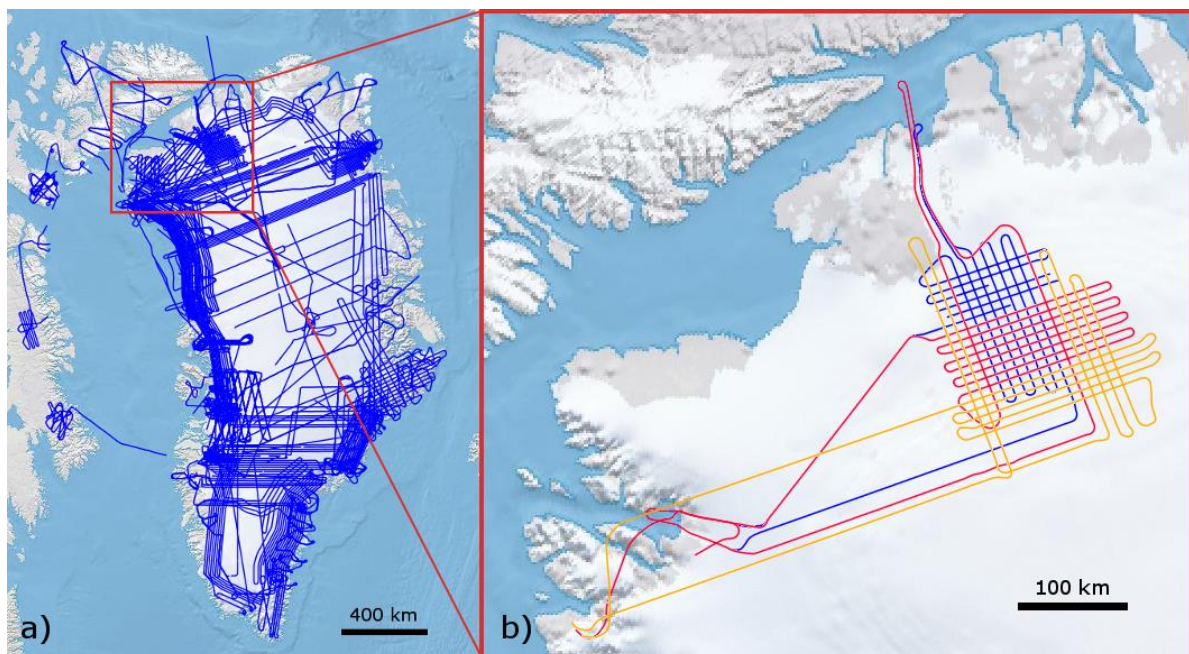
Figure 2. Map of Greenland, showing the location of the investigated region (Petermann Glacier). Taken and edited from https://ops.cresis.ku.edu/ a) Greenland and parts of Canada, with all radar missions operated by CReSIS (blue lines). The red box indicates the location of Petermann Glacier. b) Close-up of the Petermann and Humboldt catchment, displaying only the flight missions used for this thesis: mission no. 2010-03-24 (blue), no. 2011-04-29 (orange) and 2011-05-07 (red).

The main reasons for this choice are the following:

- There is a high amount of fold-like structures and deformed internal layers in this region.
- Earlier work has been done in this region; it is a region of high scientific interest.

- The data density of the region is relatively high compared to other regions where radar data has been collected. For the Petermann catchment, radar image profiles exist in an almost rectangular grid of 13 WSW-ENE striking (*horizontal*) and 12 NNW-SSE striking *(vertical)* profiles with relative narrow spacing (Figure 2b).

3   Theoretical Framework

3.1   Types of rock deformation

When a rock is affected by tectonic and gravitational forces, a *stress* is produced. The stress acting upon a surface consists of two components: *normal stress*, which is described by a vector perpendicular to the surface, and *shear stress*, which is a vector parallel to the surface (Davis et al., 2011). If the stress exceeds the strength of the rock, the rock will experience *strain* and is deformed. If straight lines within a body stay straight after deformation, and if parallel lines stay parallel, this is called *homogeneous deformation*. If this is not the case, we speak of *inhomogeneous deformation* (Reuther, 2012). One way to describe and measure processes of homogeneous deformation is to measure the *angular shear* ψ, which is the angle between the directions of a line before and after deformation. The "amount of deformation through shearing" can be described by the *shear strain* γ, which is the tangent of the angular shear: $\gamma = \tan\psi$ (Reuther, 2012). Another way to describe shear strain is by the translation of a point in shear direction (Δx) in relation to its distance to the grounding line (y): $\frac{\Delta\mathrm{x}}{y} = \tan\psi$ (Ramsay and Huber, 1987).

There are two types of homogeneous deformation: *pure shear* and *simple shear*. The difference between them can be explained by the deformation of a circle to an ellipse. At pure shear, the principle axes of strain keep their orientation, while at simple shear, their orientation changes by rotation (Figure 3). Pure shear is a deformation by compression (just normal stress, no shear stress involved), while simple shear is produced by shearing (just shear stress, no normal stress involved) (Reuther, 2012).
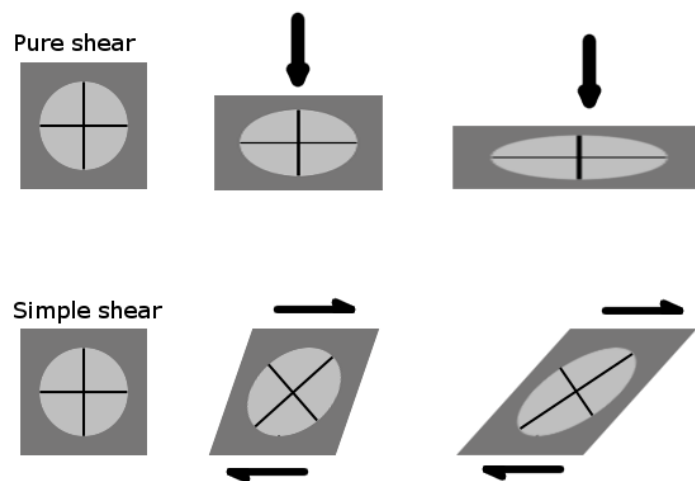
Figure 3. Pure shear versus simple shear

In nature, hybrids of these deformation types usually occur rather than just one of them, but they are useful basic types when it comes to distinguish the dominant type of strain that has occurred to a structure.

3.2 High-strain shear zone structures

A shear zone is a region of heavily deformed rocks, surrounded by regions with a lower state of finite (=total) strain. Shear zones are planar or curviplanar and are considerably longer than wide (length to width ratio has to be greater than 5:1) (Ramsay and Huber, 1987). Deformation in shear zones can either be brittle or ductile (or intermediate), depending on the rock's composition, its physical properties and the deformation mechanics acting in the single case (Reuther, 2012). Shear zones exist at all scales, they can have lengths and displacements from centimeters to hundreds of kilometers. They can appear in plate boundaries of every type and several other tectonic settings (Davis et al., 2011).

Ductile shear zones, where ductile deformation mechanisms are dominant, generally evolve in rocks at relative high temperatures and/or pressures, small strain rates and low fluid pressures – All, of course, strongly depending on the particular material being deformed. Ductile deformation is usually dominant in regions from the lower crust (underneath the brittle-ductile transition zone) to the asthenosphere under metamorphic conditions, creating rocks with metamorphic properties (Davis et al., 2011). Simple shear strain is dominant in ductile shear zones (Reuther, 2012).

Among other tectonic structures, several types of *folds* are frequent in ductile shear zones. A fold is a geologic structure that evolves when layers of rocks are bent. An upward closed fold with the oldest rocks in its core is called *anticline*, a downward closed fold with the youngest rocks in its core is known as *syncline* – Each regarded relative to the stratigraphy. Considering geometrical structures only, without knowing the geologic orientation, we speak of *antiforms* and *synforms*, respectively. Large assembled fold structures are called *anticlinoria* and *synclinoria* and can contain several (second-order) anticlines and synclines. The line connecting the points of maximum curvature within a fold is called *hinge line*. We speak of a *cylindrical fold*, if the fold's entire surface can be generated by moving the hinge line parallel to itself (Figure 4). Then the fold possesses a *fold axis*, which lies on the hinge line. If the fold does not have a fold axis, it is called *non-cylindrical* (Ramsay and Huber, 1987).
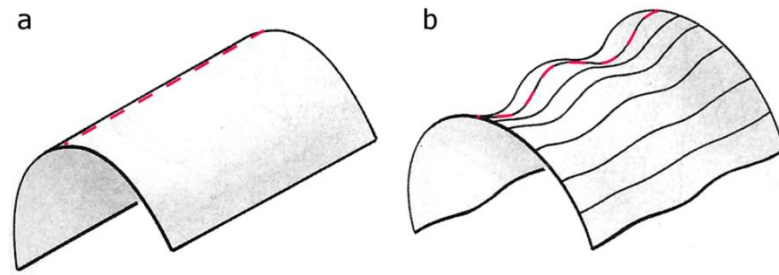
Figure 4. Cylindrical (a) vs. non-cylindrical (b) fold. Red broken lines show the approximate positions of the hinge lines. (Taken and edited from Davis et al, 2011.)

There are many ways to categorize shear zone related folds, because many different aspects such as origin and geometry can be taken into account. One possible way to categorize shear zone-related folds by their origin is the following (Carreras et al., 2005).

a) Pre-existing (e.g. buckle) folds that formed during a former deformation process and get deformed while the shearing occurs

b) Shear-related folds that form early and in planar rock fabrics, which existed even before the shearing, such as foliation or layering)

c) Shear-related folds that form late and in new, shear zone-related foliation, e.g. in mylonites, which are very fine grained rocks that form during extreme shearing (Davis et al., 2011)

(Carreras et al., 2005)
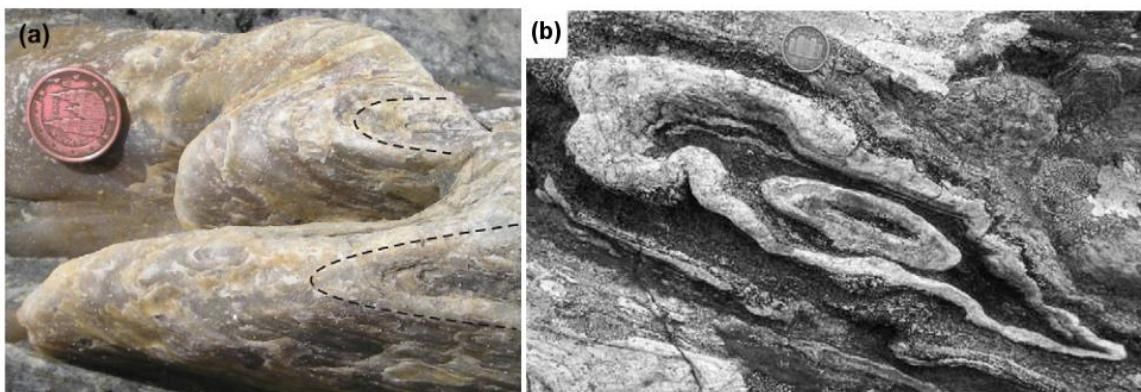
Figure 5. Photos of sheath fold structures. Coin is 15 mm diameter in each case. **a)** Intensely folded quartz mylonite layers within El Llimac shear zone, Cap de Creus, Spain. Dashed lines are parallel to hinge line (Taken from Alsop and Carreras, 2007). **b)** "Eye"-shaped structures of cross section of a sheath fold within psammites of the Moine Supergroup, Scotland (Taken from Alsop, 2006).

A type of folds that is strongly connected to intense deformation is the group of *sheath folds*. They can often be found in shear zones, but also in other environments with high strains (Ramsay

and Huber, 1987). Sheath folds are non-cylindrical folds with a strongly curved hinge line and a conical, rounded shape (Figure 5a), resembling the shape of a wind sack (Davis et al., 2011). In outcrops, they often are visible as typical elliptical "eye"-shaped structures (Figure 5b). Sheath folds can belong to group a) or c) mentioned above: They can either develop if older folds, which existed prior to the onset of shearing and have slightly bent hinge lines, get sheared (Ramsay and Huber, 1987; Carreras et al., 2005), which is group a) mentioned above. However, most sheath folds found inside shear zones nucleate during the shearing itself, at first with a high angle between shear direction and hinge line, but with ongoing deformation the axial surface of the fold rotates towards the shear direction, sometimes even until shear direction and fold axis are nearly parallel (Figure 6 and Carreras et al., 2005).
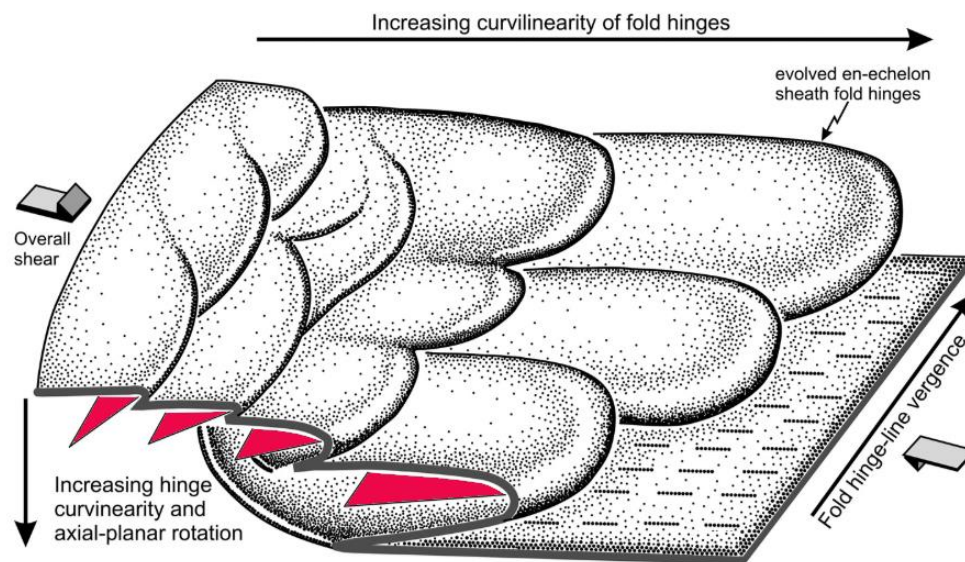
Figure 6. Schematic cartoon illustrating the evolution of sheath folds, with an early stage on the left and fully evolved sheath folds on the right. The fold axis is highlighted in red to emphasize the development of the angle between fold axis and orientation of the shearing (Taken and edited from Alsop and Carreras, 2007).

Sheath folds evolve in many different environments and materials, e.g. salt diapirs, metamorphic rocks in shear zones and soft-sediment settings, such as slumps (Alsop et al., 2007). Even in glacier ice sheath folds have been located (Goodsell et al., 2002). Also, they can appear at all scales, with lengths from millimeters to tens of kilometers and undergo a large variety of deformation processes. Sheath folds can show different geometries, but these geometries are to be independent from scale, material and properties such as viscosity, as similar geometries can occur in highly variable settings. Important constrains are the geometry prior to the creation of the sheath folds (e.g. folds being present before, as in group a) mentioned above) and the nature of deformation (Alsop et al., 2007). The appearance, ellipticity and inner geometry of the "eye"-shaped

cross sections give information about the deformation type, whether it is mainly associated with simple shear (as in shear zones), general shear (which is simple shear and pure shear combined) or rather possess a compound of a constrictional sort of deformation (Alsop and Holdsworth, 2006; Ez, 2000).

In summary, it is important to emphasize that sheath folds in shear zones can either evolve from older (buckle) folds or nucleate during the shearing itself. The appearance of sheath folds is possible in a large variety of materials, scales and geological settings, if high strains are present.

3.3   Properties of ice

The following properties of ice are important when dealing with deformation of ice and the development of folds in ice layers. Glacier ice has a density of 830-910 kg/m³ (Benn and Evans, 2010), which is much lower than most other rocks and minerals – For comparison: Quartz has a density of ca. 2650 kg/m³. Its melting temperature lies around 0 °C. Ice temperatures under natural conditions vary from -40 °C to 0 °C (Benn and Evans, 2010), very close to its melting point, so this is another remarkable difference to most other rocks on earth's surface.

Ice is highly anisotropic, which means that its physical properties depend on its crystallographic orientation.

When the accumulation of snow exceeds its ablation, a glacier forms. Glaciers and ice streams transport the snow and ice that accumulates all about the ice sheet toward the coast, where they calve into the sea. The balance ice velocities of the Greenland Ice Sheet vary from tens to hundred meters per year in the interior, and from hundred up to ten thousand meters per year in within the fast-flowing glaciers at the margins (Benn and Evans, 2010).

3.4   Radar techniques in polar research

The general principle of radio detection and ranging (*radar*) measurements is the following: Electromagnetic waves with a frequency within the radio spectrum are being transmitted toward a target. A small amount of these waves are reflected from the target and detected by a receiver antenna. From the time between emission and detection of the radar signals, one can determine the distance between antenna and target. The frequency of radar waves used for present-day polar research commonly ranges from hundreds of MHz to tens of GHz, for instance the frequencies CReSIS uses in its radar measurements vary from 160 MHz to 18 GHz (Rodríguez-Morales et al., 2014).

For ice sheets, such measurements are usually done from an aircraft. Reflecting targets are the ice surface, the bedrock, and every internal ice layer where the significant properties – depending on

the propagation of electromagnetic waves - of the media change (Gogineni, 2012). In order to get proper depth data (and hence profile images) of the ice sheet out of the travel times of the waves, several calculations and corrections are needed.

A very important issue is the varying properties of the signal different wave frequencies produce. A high frequency (in the range of GHz) provides a high vertical resolution, but leads to only a small maximum measurement depth, because of the attenuation of radar waves within the ice. Thus, high frequencies are used for surface-near investigations. Accordingly, low frequencies (in the range of MHz) provide a high maximum measurement depth, but only a low vertical resolution. These frequencies are used for example examining the position of the bedrock (Rodríguez-Morales et al. 2014).

Because radar waves get attenuated while propagating in ice, the signal of the ice bottom (the bedrock) is much smaller than the signal from the ice surface (Gogineni, 2012). To be able to capture both signals anyway, the gain of the receivers has to be dynamic. The recently used method here is called a *waveform playlist*, which allows using low and high gain channels at the same time. Two different waveforms – one with long and one with short pulse duration – allow multiplexing these different receiver gains over time, because no time penalty occurs. The short pulse duration (e.g. 1 μs) used with low receiver gain is used for the ice surface capture; while the long pulse duration (e.g. 10 μs) combined with high receiver gain is used for the bedrock surface. The latter is more sensitive, but the signal is generally saturated und therefore not usable for the ice surface. If the measurements are done from a high aircraft altitude, it is also possible to use only one single, high receiver gain (Gogineni, 2012).

In order to process the measured data – which consist of travel-time values – one has to assume a value for the dielectric permittivity of the ice. The relative permittivity, or *dielectric constant*, ε_r characterizes the ability of a material to let electromagnetic waves pass through it, compared to this ability of a vacuum. However, the dielectric constant of ice is not constant, but depends on multiple parameters, such as crystal orientation, density, acidity and temperature of the ice, and also on the frequency of the deployed electromagnetic waves (Fujita et al., 2000).

4   Materials and Methods

The proposed 3D model of the ice sheets of Petermann Glacier was mainly created using the 3D modeling program MOVE by the Midland Valley company. Therefore, CReSIS' radar images showing the internal ice layers were imported into MOVE and prominent ice layers that can be followed along the entire region were picked in order to create 3D surfaces from them.

4.1   CReSIS' Radar Depth Sounder products

4.1.1   CReSIS' radar instrumentation in general

Since 1993, CReSIS has been flying several polar research missions with grant support of the NSF (National Science Foundation) and NASA (National Aeronautics and Space Administration), collecting radar data of Greenland, Canada and Antarctica. Therefore, various radar instrumentations were used, sometimes within the same mission at once. The main difference between these measuring instruments is the frequency of the radar waves used for each method:

- High frequencies lead to only a small maximum measurement depth, but a high vertical resolution. This is used for surface-near investigations, for example by the Ku-band Radar, which uses frequencies of 12-18 GHz, has a maximal measurement depth of 10 m and a resolution up to 4 cm. It is used for accurate measuring of the ice surface and also for the upper snow layers (Rodríguez-Morales et al. 2014).

- Low frequencies provide a high maximum measurement depth, but only a low vertical resolution. These properties are for example used for Radar Depth Sounder (RDS) data, which this thesis is focused on. It uses radar waves with frequencies of 160-230 MHz and reaches measurement depths of up to 4 km with a resolution of 6 m or 20 m (depending on aircraft used, see below), so it is well-suited for sounding and imaging the ice-bedrock interface and deep internal layering of the ice (Rodríguez-Morales et al. 2014).

Further radar investigation methods of the CReSIS missions are the *Accumulation Radar* (600-900 MHz, for internal layering and shallow ice thickness) and the *Snow Radar* (2-8 GHz, for snow cover and internal layering) (Rodríguez-Morales et al. 2014). Thus, a large span of the radar frequency spectrum is used by polar research, covering two orders of magnitude (factor 100).

4.1.2 Radar Depth Sounding (RDS) of Petermann Glacier

In the following explanations about RDS, I will focus on the techniques used in the two CReSIS missions that I used for my model. They used different aircrafts as well as different generations of the Multi-Channel Coherent Radar Depth Sounder (MCoRDS) system.

For my 3D model, data of the following CReSIS missions were used:

- **2010 Greenland DC8** (*NASA DC-8 Airborne Science Laboratory* aircraft), *MCoRDS* system; flight 2010-03-24
- **2011 Greenland P3** (*NASA P-3B Airborne Science Laboratory* aircraft), *MCoRDS 2* system; flights 2011-04-29 and 2011-05-07. (Gogineni, 2012)

The number of a flight always displays the date when it was being carried out, in YYYY-MM-DD (i.e. year-month-day) pattern.

For achieving a dynamic range of receiver gain, the waveform playlist method was used, which I explained in chapter 3.4 – Radar techniques in polar research. In both systems, MCoRDS and MCoRDS 2, a frequency bandwidth of 180-210 MHz is theoretically usable, but the DC-8 platform used for 2010's mission restricted the bandwidth to 189.15-198.65 MHz. This narrower frequency bandwidth (9.5 MHz in 2010's mission, while 30 MHz in 2011's mission) leads to a slightly worse range resolution of the radar, which is the minimum range difference that is needed to distinguish two targets from each other (Gogineni, 2012). Despite varying for the different missions, the range resolution is considered good either way (Gogineni, 2012), being 0.7 m in the worst case.

Also the along-track resolution is relative good, with about 25 m for all missions. It stays constant for all systems, because it only depends on the processing, which did not change.

A more serious problem is the cross-track resolution (vertical down into the ice). Like the range resolution, it depends on the frequency bandwidth, but also on the flying altitude, the thickness of the ice, the roughness of the bedrock's surface and the beamwidth of the antenna. A higher altitude, thicker ice, rougher surface and a bigger beamwidth result in a lower resolution. The difference between the flight missions lies in the antenna bandwidth: The DC-8 platform used in 2010 has a beamwidth on 53.1°, while the P3 platform used in 2011 has a beamwidth of only 16.6° (Gogineni, 2012). The difference in beamwidth results from the different number of elements the antennas consist of and the spacing between the elements. For DC-8 (2010), there are 5 elements with a spacing of 0.25 m, while P3 uses 7 elements with a spacing of 0.5 m. Finally, for an assumed flying altitude of 500 m and an ice thickness of 2000 m, there is a cross-track resolution of 620 m for the P3 platform (2011's mission), but only of 2237 m for the DC-8 platform (2010's mission), which is 3.6

times as high as for P3. This large difference of cross-track resolution is clearly visible in the radar images.

For processing the data – which means converting the measured travel times to depths within the ice sheet to be able to create images from them – it is necessary to assume a value for the dielectric constant ε_r of ice (see chapter 3.4 – Radar techniques in polar research). For this purpose, an estimated value of $\varepsilon_r = 3.15$ was used, considering the ice being uniform, including the upper regions that consist of firn. Corrections for temperature, density or frequency of the applied waves were not performed. For the dielectric constant of typical dry ice, an error of 1 % is expected (Fujita et al., 2000). This results in an ice thickness dependent error of 0.5 %, e.g. 10 m for an ice thickness of 2000 m (Gogineni, 2012).

4.1.3   The produced radar images of the considered region

The images produced from the radar data (and the data itself) are provided online on CReSIS' data website under the URL https://data.cresis.ku.edu/. The images are labelled using the flight date, the segment number and the frame number (e.g. 20110507_01_029, which means frame no. 29 of segment no. 01 from the flight of 07.05.2011). A segment is part of a flight, where the radar settings do not change. Segments are divided into several frames of about 50 km length to provide the data and images in manageable parts (Gogineni, 2012).

The provided pictures are exaggerated at a factor around 10. This factor is not constant, but depends on the length of the particular frame. On the x-axis, the distance along flight track (in km) is displayed, together with latitude and longitude. On the y-axis, the depth under ice surface (in m) is displayed. The zero-meters-line is settled to the mean position of the ice surface of the single frame.

The chosen images show the ice layers down to the bedrock. Especially within the sharp images, distinct isochronous layers are visible, of which several can be followed over the entire region. From ice surface to bedrock, the layers can be divided into several parts, according to their appearance in the radar images (Figure 7).

a) Quite undisturbed ice layers, appearing grayish in the radar images.
b) Depending on location, undisturbed to folded, disturbed ice layers, appearing brighter in the radar images.
c) Disturbed, "fuzzy" ice, no layering visible.
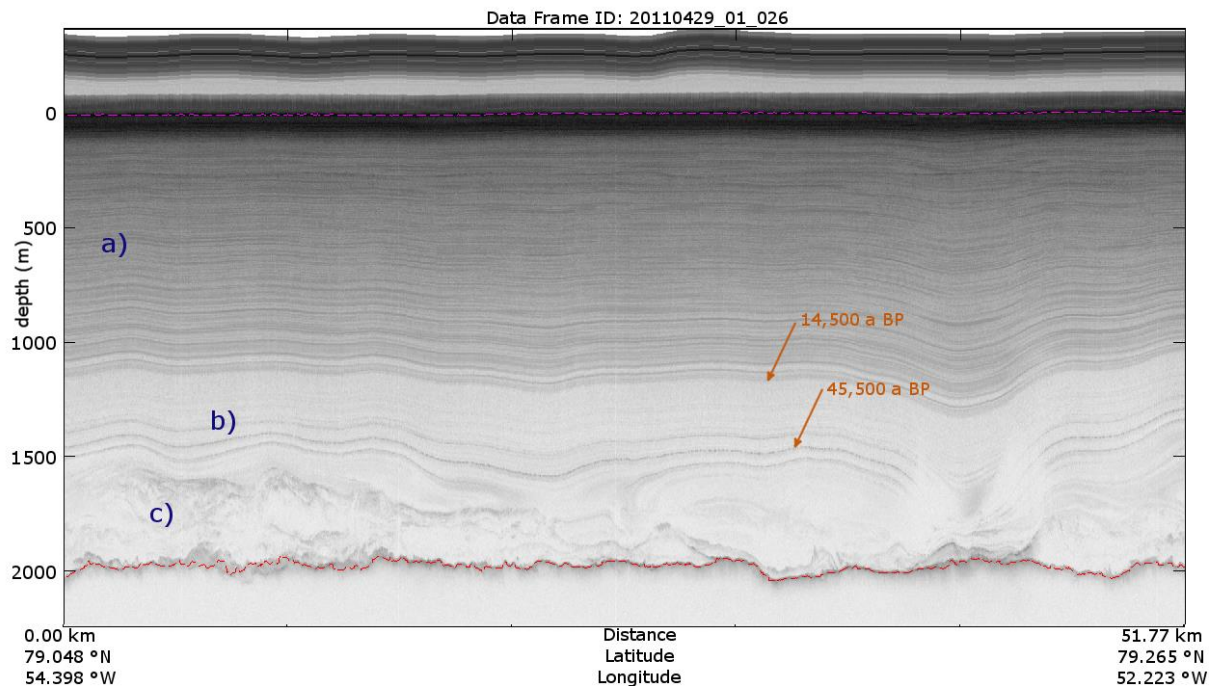
Figure 7. Radar image illustrating the main parts of the ice, labelled a) to c) and the ages of certain ice layers. See text for explanation. (Taken and edited from Gogineni, 2012.)

The ice layers of part a) have been dated to be mostly from the current Holocene interglacial period. The lower bound of this grayish part is dated to 14,500 years BP (Figure 7 and NEEM homepage). This horizon was picked for the creation of the 3D model (see chapter 4.3 – Creation of the 3D model). The ice of parts b) and c) mostly belongs to the last glacial period, which lasted from 115,000 to 12,000 years BP. The lowermost ice of part c) even was accumulated during the Eemian interglacial period (older than 115,000 years). Within part b), there are three very distinctive "highway"-shaped layers, which can be followed over the entire area. The middle of the three layers is dated to 45,500 years BP (Figure 7 and NEEM homepage) and was picked for the 3D model, too.

Due to different cross-track resolutions, the quality of the images derived from 2010's data show perceptible deviations from the quality of the images of 2011's mission. Relatively detailed internal ice layer reflections are visible down to the bedrock in 2011's images, but in the images of 2010, one can distinguish thicker and more prominent layers only. Often, the boundary between thick blocks of ice is not clearly visible, but rather blurred and not sure to determine. Radar disturbances, such as double signal reflections of the ice surface, are more pronounced in 2010's images, too (Figure 8).
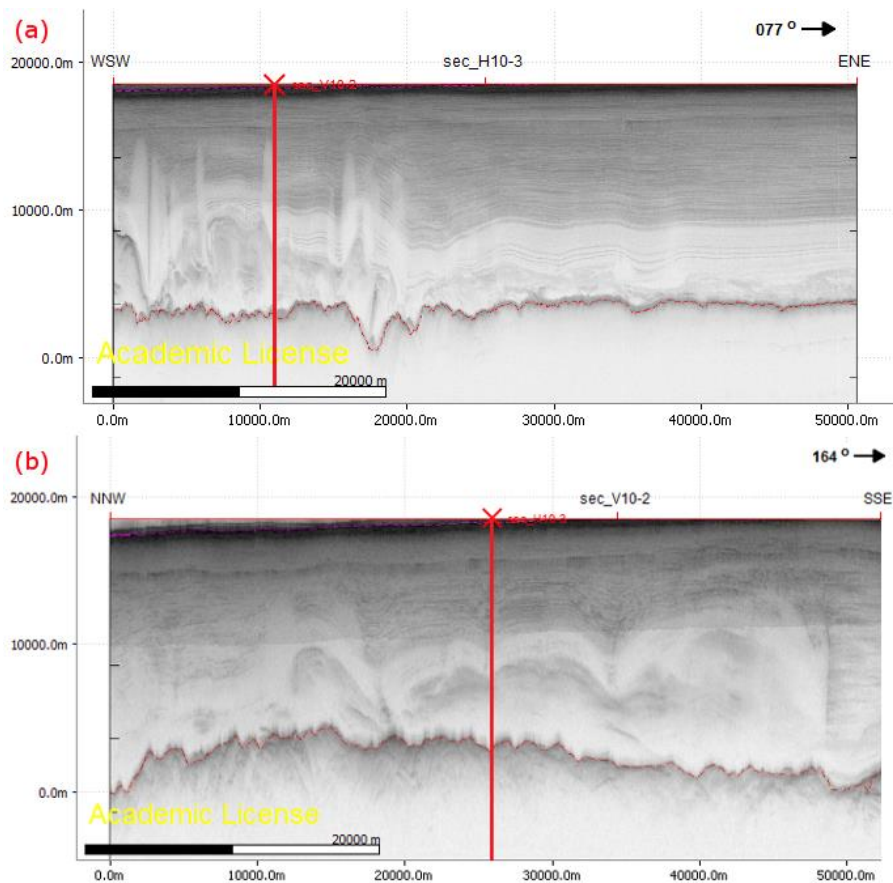
Figure 8. Two RDS images that intersect at the shown red line: **(a)** Frame no. 20110507_01_029 is of rather high quality, several single ice layers can be clearly distinguished. **(b)** Frame no. 20100324_01_011 is of rather low quality, only larger ice blocks are distinguishable, but still with no sharp boundaries. A radar artifact (double reflection of the ice's surfaces) cuts the layers horizontally.

4.2   Handling of images and data

Before the 3D model could be created, several modifications to the existing RDS images and data had to be made. A list with the file numbers of the images used for the creation of the 3D model can be found in the appendix.

4.2.1   Cutting the images' horizontal extent

Since only straight profile sections are usable for the model, the images had to be cut at the ends where the aircraft flew a bend and the section is curved. To find out if a section is straight, the latitude- and longitude-values of every measuring point (provided in .csv files on the CReSIS data product website) were plotted within an Excel-diagram. By adding a linear trend line and considering the coefficient of determination R^2 ($R^2=1$ means perfect fit, $R^2=0$ means no fit at all), it was decided if the section is straight enough: R^2 of 0.9996 and greater were accepted as sufficient. For the correct insertion of the images into MOVE, the geographic coordinates of their margins have to be known. If a section has to be cut, there is only the possibility to cut off multiples of 20% of the profile, because the latitudes and longitudes are only displayed after every fifth of the width of the provided images

(Figure 9). The coordinates of other positions in the image could be estimated, but this would be a possible error source. Because the exact positioning of the images is more important than a possible – only little – increase in the model's region's size, it was decided to proceed the way outlined above. The cutting of the images was done with a simple image editing software. Detailed information about which images were cropped how much can be found in the appendix.
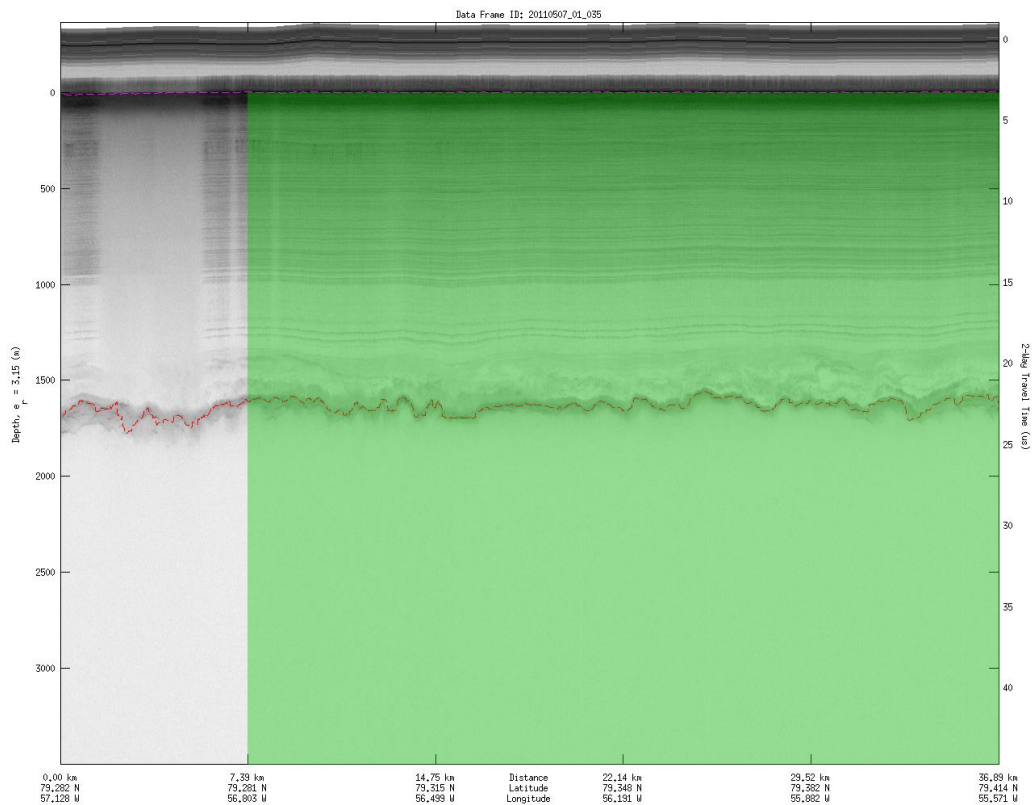
Figure 9. Original RDS image frame no. 20110507_01_035, illustrating how the images were cut before inserting them. The green box marks the part of the image that was inserted to MOVE. See text for further explanations. (Taken and edited from Gogineni, 2012.)

4.2.2 Cutting the images' vertical extent

For the insertion of the images into MOVE, also the depth values of the upper left and lower right corners of the images have to be known. While the lower margin of the depth axis is always located at 3500 m depth, the upper end varies. As the upper value is not visible in the pictures – the axis is only labeled in steps of 500 m – the upper margin has been cut down to the 0 m line, which marks the mean position of the ice surface of the picture (Figure 9).

4.2.3 Projection and DEM

The geographical coordinates of the margins of the images are originally given in latitude and longitude, which depict a spherical projection system. As MOVE uses rectangular geometry, the

coordinates of the images' margins were converted into the projection Bamber et al. (2013) used for their bed elevation dataset. It is a polar stereographic projection with standard parallel at 71 °N and a central meridian of 39 °W (Bamber et al., 2013). A digital elevation model (DEM) and bedrock elevation grid derived from the dataset of Bamber et al. (2013) have been added to my model in MOVE to be able to look at the ice structures in relation to topography and bedrock, too. Hence it was the best solution to use this projection for the creation of the model. The coordinates of the images' margins can be found in the list of the images in the appendix, in latitudes and longitudes as well as in the converted Bamber projection data.

While creating the model, it was discovered that the used radar images do not match the DEMs. Some images are tilted towards the south (Figure 10). This effect mostly occurs in the northernmost part of the region, where the ice surface is most inclined. This problem presumably comes from diverse data processing methods used for the creation of the DEMs and the images, respectively. For getting to know the precise reasons, a close look to the respective processing codes would be needed. As such investigation would exceed this thesis' topic and the tilting problem could rather easy be solved within the model creation process (see chapter 4.3.4 – DEMs and tilting from page 23), it is refrained from examining this issue further.
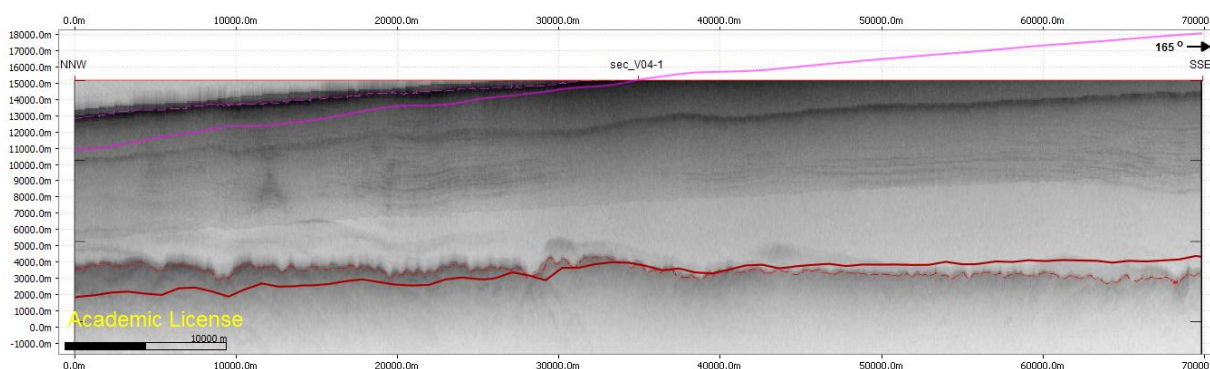
Figure 10. An example for the issue that the radar images are tilted, comparing the DEMs of bedrock to the ice surface. Dashed lines show ice surface and bedrock on the image, solid lines are intersection lines with the DEMs. The image is frame no. 20100324_01_034 from the north western edge of the examined region, striking NNW-SSE.

4.3   Creation of the 3D model

In this chapter, I present the main processes that were done to create the 3D model in MOVE. Detailed step-by-step explanations can be found in the appendix.

4.3.1   *Importing the radar pictures into MOVE*

The first step was to insert the edited radar images into MOVE. As the used images are arranged in a grid of WSW-ENE striking (horizontal) and 12 NNW-SSE striking (vertical) sections, it seemed reasonable to name the sections with a letter for the orientation (H for horizontal and V for vertical)

and a number ascending from north to south and west to east, respectively. Because every section

consists of more than one image, and every image gets its own section when inserting into MOVE,

the resulting sections get a second number according to their order. An example for the name of a

section is sec_H13-3 (Figure 11).
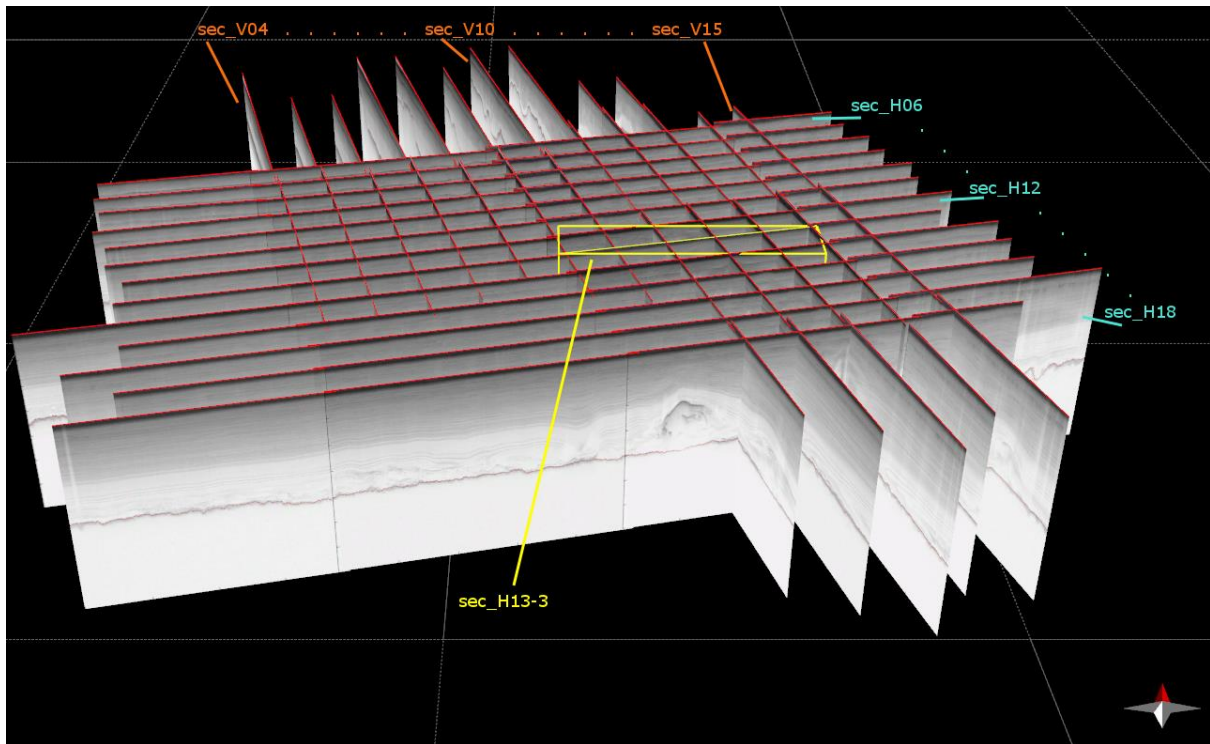
Figure 11. A screenshot of all RDS images after inserting them into MOVE, illustrating the labeling of the sections. Background grid unit is 100 x 100 km.

The edited radar images were imported into MOVE using the coordinates of the upper left and

lower right edge. The model was created with an exaggeration of 10, so I used the original values

multiplied by 10 for the vertical z-values (depth) while importing the images.

Afterwards, the profiles had to be adjusted manually in matters of their vertical position, because the

labeled level of 0 m depth differs, as it is at the mean ice surface level of each single image. This was

done by looking at prominent ice layers and joining the pictures where they apparently match.

4.3.2   Picking prominent layers

Two distinct ice layers were picked that can be followed along the entire region, using the tool

Create Lines – Horizon in MOVE. In the attached model, they are organized as horizons named

gray_bottom and *triple_mid*. Thirdly, several prominent structures within the lower, heavily

disturbed part of the ice were picked, all assembled in a horizon called *strucs_mix*. While

gray_bottom and *triple_mid* display a specific ice layer each, *strucs_mix* does not contain structures

that belong to one single ice layer, but sums up miscellaneous striking structures. For the sake of

clarity, each horizon is depicted in a particular color (Figure 12). Several color shades were used to indicate variable reliabilities of the picked lines (Table 1).

Table 1. Overview of the horizons that were picked for the creation of the model, including the reliability, the name of the horizon in the model and the color shade used.

Horizon	Reliability	Name in the model	Color shade
gray_bottom	high	gray_bottom	dark blue
	medium	gray_bottom_bad	light blue
triple_mid	high	triple_mid	magenta
	medium	triple_mid_bad	purple
	low	triple_mid_guess	orange
strucs_mix	variable	strucs_mix	green
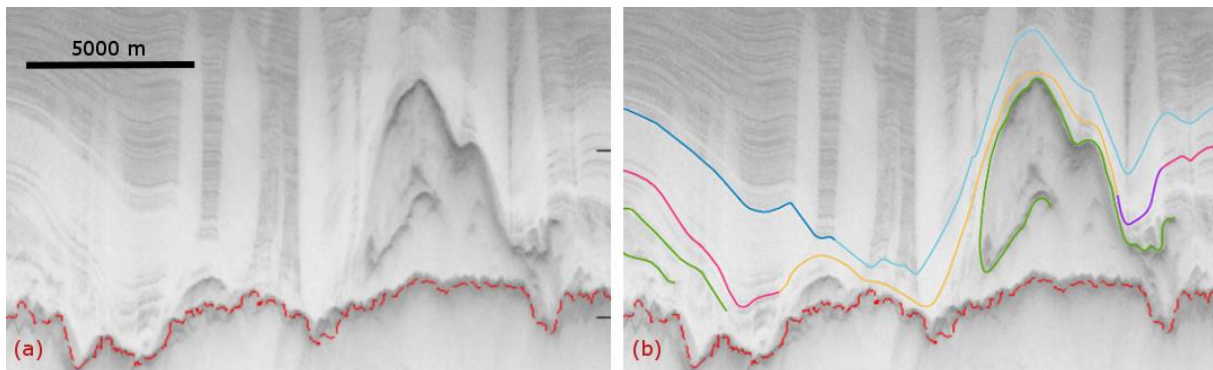
Figure 12. Detail of Section H09-2 (frame no. 20110507_01_025, before (a) and after (b) picking the horizons. All horizons and reliability levels occur in (b), depicted in different colors: Horizon *gray_bottom* in dark blue and light blue for high and medium reliability, horizon *triple_mid* in magenta, purple and orange for high, medium and low reliability and horizon *strucs_mix* in green for several prominent ice layers further down, with variable reliability.

The reliability levels (high – medium – low) can be differentiated as follows.

- A **high reliability** means that the position of the surface is clearly visible in the radar image, either in the original image or after editing it as mentioned above.

- A **medium reliability** means that the position of the surface is not clearly visible in the image, but very likely to be at the picked position, considering parallel running layers and the fact, that the often occurring "white areas" in the radar images mostly are founded in the fact that the ice layers are too steep to return the radar signal.

- A **low reliability** means that the position of the surface is very hard to determine, because the ice layers are rather disturbed in this region and no clues can be inferred

from the adjacent layers. Nevertheless, these parts of the horizons have been picked, because there was no evidence for an interruption of the ice layers at these positions. It is not totally sure if these horizons are present in these regions, but if they are, then most likely on the picked positions.

To enhance the quality of the radar images, the image processing program *ImageJ* has been used, mostly its tools *Enhance Contrast*, *FFT – Bandpass Filter* and *Lookup Tables*. These image editing methods regarding contrast and color distribution helped to recognize distinct ice layers (Figure 13).

After all lines were picked, a first impression of the structures within the ice layers can already be received (Figure 14).
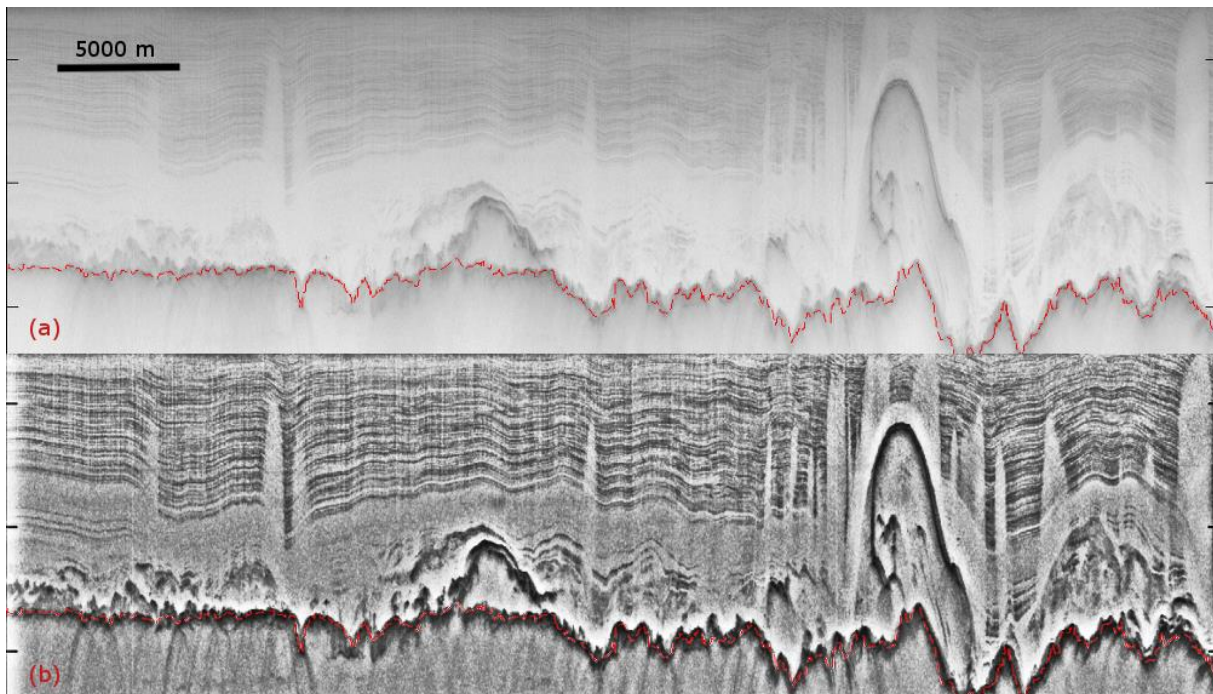
Figure 13. RDS frame no. 20110507_01_012, before (a) and after (b) applying contrast tools of the program ImageJ, as an example for enhancing the image quality to be able to recognize distinct ice layers better
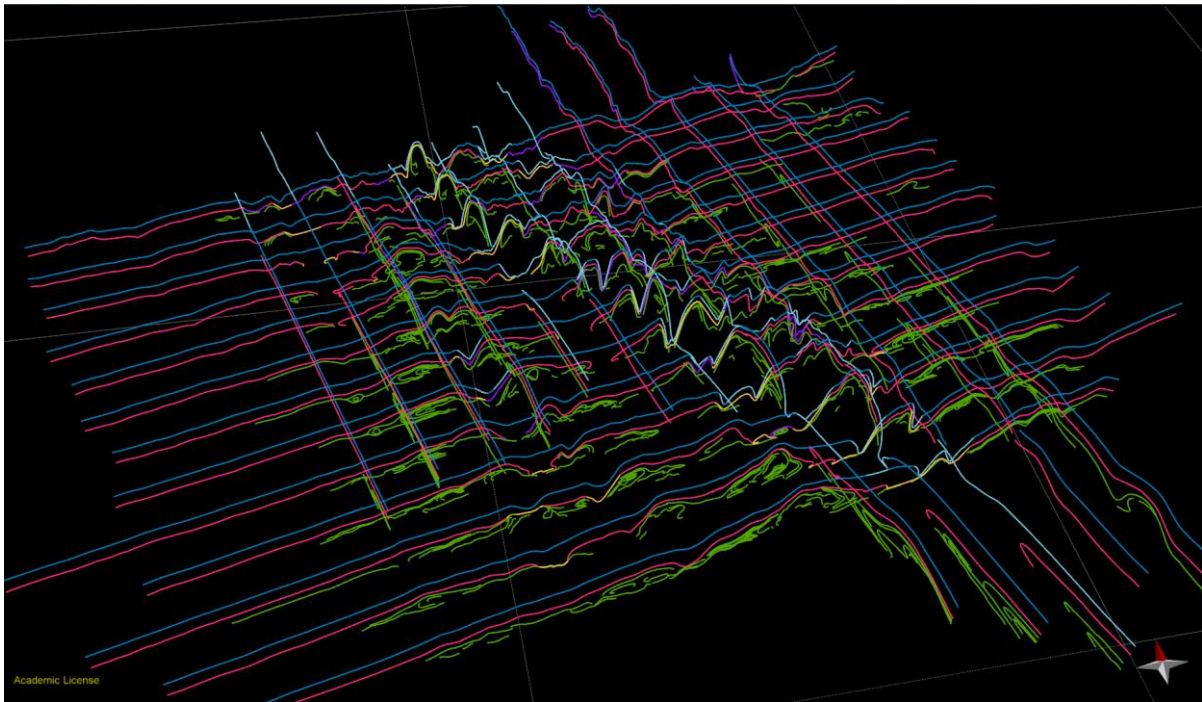
Figure 14. All horizons picked for the creation of the model. For color explanations, see text.

4.3.3   Creating surfaces from the layers

The 3D surfaces of the horizons were created with the "Linear"-method of the *Create Surface From Lines* tool, using the lines of the horizontal (WSW-ENE striking) sections. The vertical lines were not used for the calculation of the surfaces, but as reference for the position of the layers and the shape of the surface. The piercing points of the horizons picked in the vertical sections through the horizontal sections were displayed as crosses (Figure 15). If their position differed significantly from the position of the horizons picked in the horizontal sections, the involved images were compared and decided which position seems more reasonable.
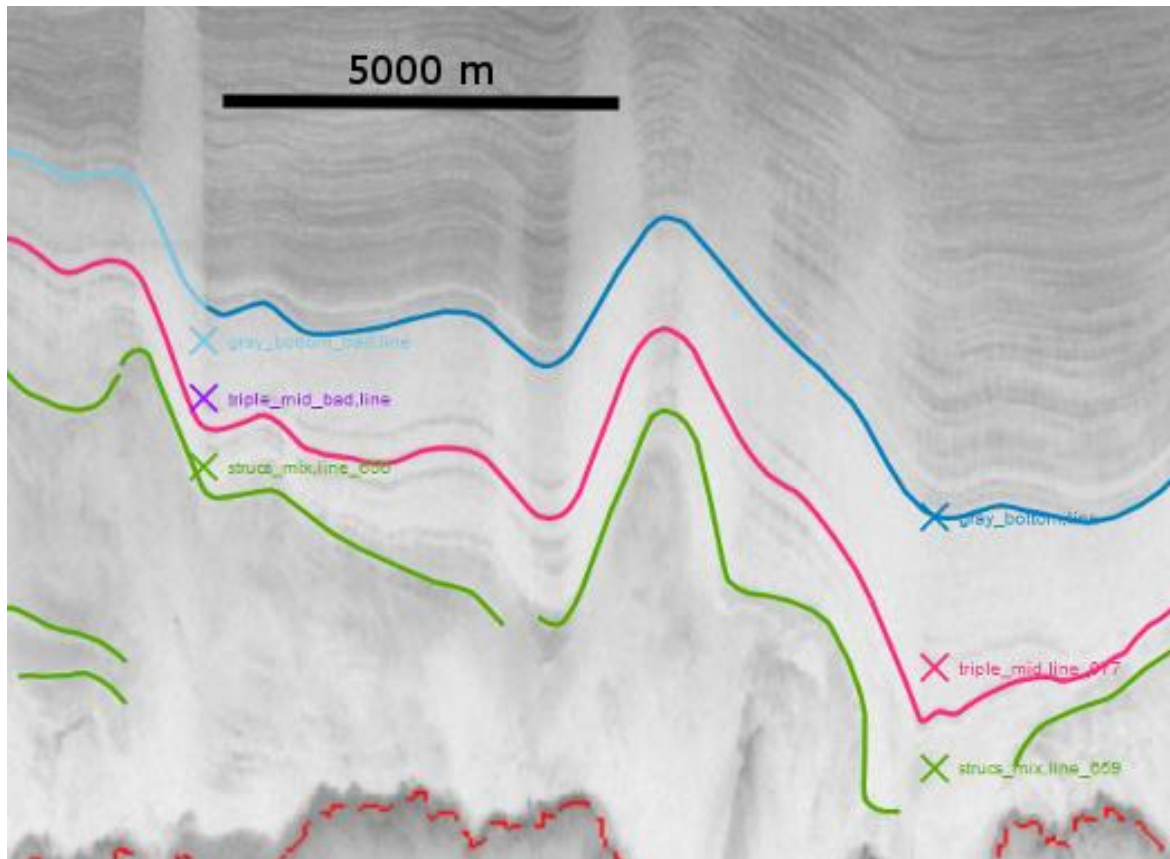
Figure 15. Detail of section H10-3 (frame no. 20110507_01_029) with intersection points of perpendicular sections (sec_10-2 and sec_11-2) displayed.

The correlating lines of adjacent horizontal sections were connected and smoothed at the borders, where inconsistencies sometimes could be found. To simplify the handling of the horizons, adjacent horizontal sections were joined to one long section, e.g. sections H08-1, H08-2, H08-3 and H08-4 were combined to Section_H08. The horizon lines were resampled to a sample interval of 50 m in order to get smooth surfaces from them.

The "Linear"-method connects neighboring horizons with straight lines, taking all control points of the horizons into account, and creates a grid of little triangles between them (see MOVE help-file). However, if you created a surface between two horizons using all lines at once, MOVE would not always connect the points that belong together, because it mostly connects opposite points regarding the length of the lines, not their shape. The more variable and folded the lines are, the more complicated the creation of proper surfaces becomes. Hence, the horizons had to be cut to parts of which the endpoints most certainly fit together. This was determined by having a close look to the radar images to identify distinct features of the ice layers in adjacent images, e.g. prominent bends and folds. Additionally, the horizons picked in the vertical sections provided a first impression about how the surfaces must be shaped (Figure 16).
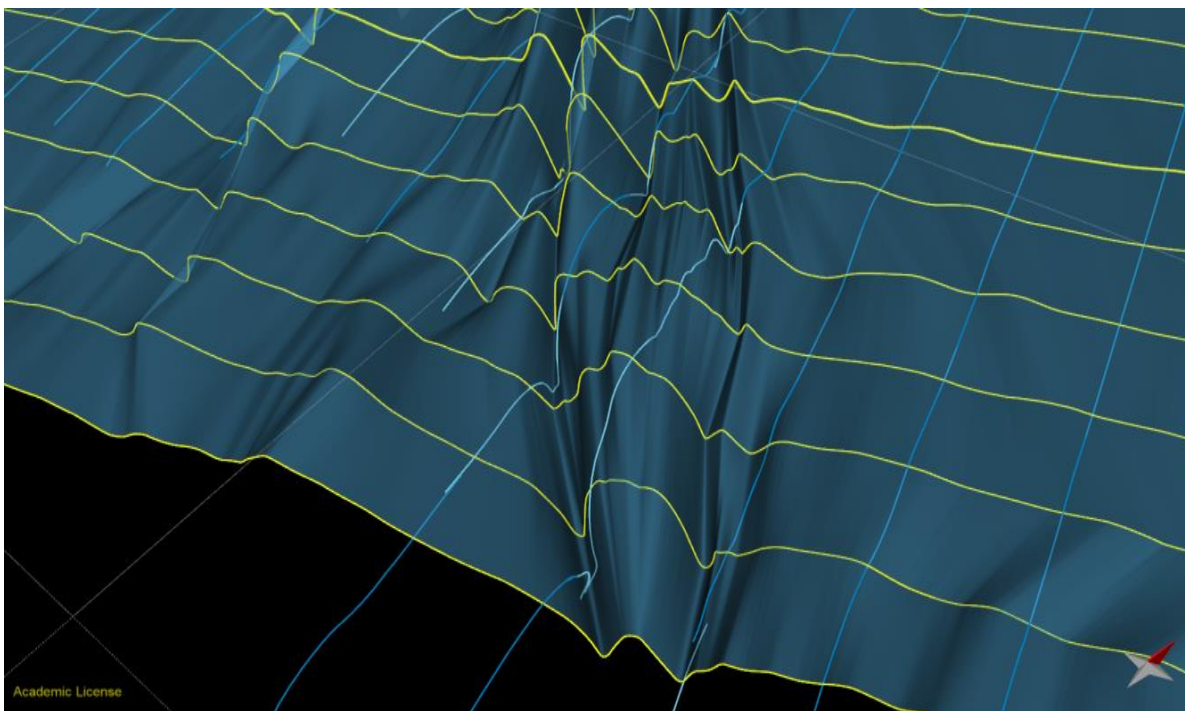
Figure 16. While the lines of the horizontal sections (here depicted in yellow) were used to generate the surfaces, the lines of the vertical sections (depicted in shades of blue) helped to consider the right direction and which parts of the "horizontal" lines should be connected in order to create a surface.

As the lines had to be connected and cut again, and could not keep their different colors, horizons with a high and medium reliability were combined to one category in order to create surfaces from them. If horizons of low reliability were involved – which affects horizon *triple_mid* only – the surfaces created from them were assigned a color different from those created from higher reliabilities.

4.3.4   DEMs and tilting

A digital elevation model (DEM) of the topography was added to the model, as well as a DEM for the bedrock, generated by the dataset compiled by Bamber et al. (2013). Additionally, a velocity grid showing the absolute surface ice velocities was added to the model, using the data of Joughin et al., 2010.

Since the radar images – and thus, all horizons and surfaces created from them – turned out to be tilted towards the used DEMs of bedrock and ice surface, it was decided to tilt all created horizons and surfaces back, to be able to look not only at the surfaces in relation to each other, but also compared to bedrock and ice surface. For doing this, it was necessary to reorganize the horizons, so that they were no longer arranged in sections. The radar images themselves were not tilted, because MOVE allows straight vertical images only. To be able to match the model to the DEM, I picked

several lines of the bedrock, as it appears in the radar images. This was mainly done at the borders of the region.

The horizons and surfaces were tilted as a whole, 1.35 ° to the north and 0.98 ° to the west, using the center of the dataset as center of rotation. The rotation was done manually until the picked bedrock of the radar images matched the slope of the bedrock's DEM. Afterwards, the model had to get translated 1,000 meters downwards (along the z-axis) to fit the position of the bedrock and ice surface DEMs.

4.3.5 Provided model files

The model is provided in three versions:

1) petermann_horizons.mve

This version contains the original picked horizons, without any surfaces, containing the color code for reliability of the lines. This file is convenient to get information about the trustworthiness of the lines.

2) petermann_surfaces.mve

This version shows the rearranged horizons (high and medium reliability combined) and the surfaces that were developed from them. The horizons are still organized within the sections, but horizons and sections are not tilted yet. This version is suitable to get an impression of the three-dimensional shape of the internal ice layers in relation to each other.

3) petermann_after_rotation.mve

The third version contains the re-tilted horizons and surfaces, but no arrangement within sections anymore. This version is helpful to be able to compare the position of the internal ice layers to the bedrock and ice topography.

5   Results

The result of this thesis is a 3D model of ice layers within the Petermann catchment consisting of mesh surfaces. Additionally, several cross sections have been added to the model, which provide a better view at specific structures. Some of these sections are shown at the end of this chapter.

Two ice layers have been visualized as 3D surfaces over the entire area: The bottom of the layers appearing gray in the radar images, which has an age of approximately 14,500 years, was relative easy to follow over the entire region. The result is a 3D surface (**gray_bottom**) without any gaps, containing of 260 small mesh surfaces (Figure 17a). Secondly, a prominent layer of an age of approximately 45,500 years was constituted over the entire area, but with gaps where the layer could not be found, and with surfaces of low reliability, where it is unclear if the layer is present or not. It contains of 183 small mesh surfaces of high and 71 mesh surfaces of low reliability and is called **triple_mid** (Figure 17b).
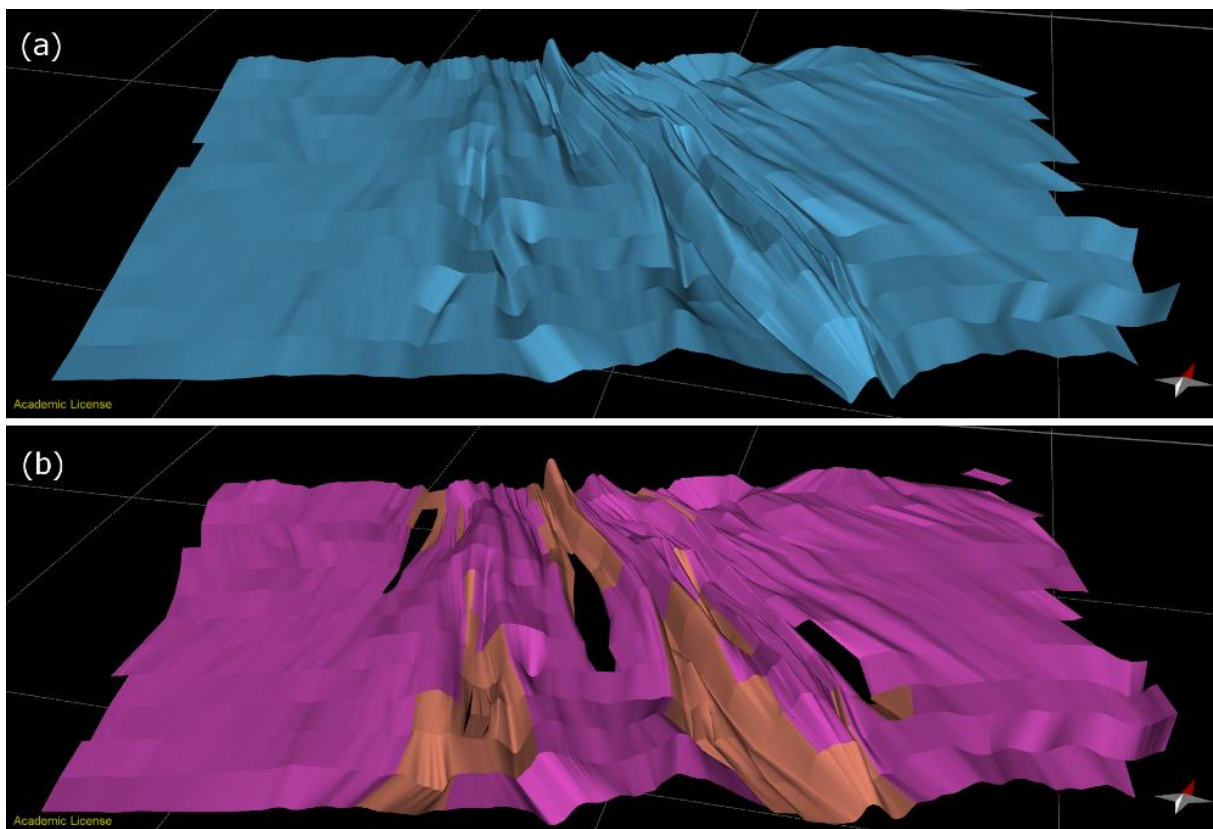
Figure 17. All mesh surfaces created from the horizons, slanted view from above. **(a)** horizon gray_bottom and **(b)** horizon triple_mid. Background grid unit is 100 x 100 km.

By looking at the overall shape of the ice layers, long fold belts can be observed. This is most obvious in gray_bottom surface, but triple_mid's large-scale structures resemble those of gray_bottom, too. The folds generally strike towards the flow direction of Petermann Glacier, varying

from NW-SE to almost N-S. The height and steepness of the folds varies along as well as across flow, but generally the folds tend to get tighter and steeper in the middle of the area and towards the outlet of the glacier (Figure 18 and Figure 19). The folds can be mostly described as near-cylindrical, with only slightly curved hinge lines. Towards flow direction, the folds mostly do not propagate straight, but rather slightly curved. The fold areas vary in across-flow width, some growing narrower, others growing wider in flow direction. Some fold areas taper until they merge into the adjacent areas (Figure 19).
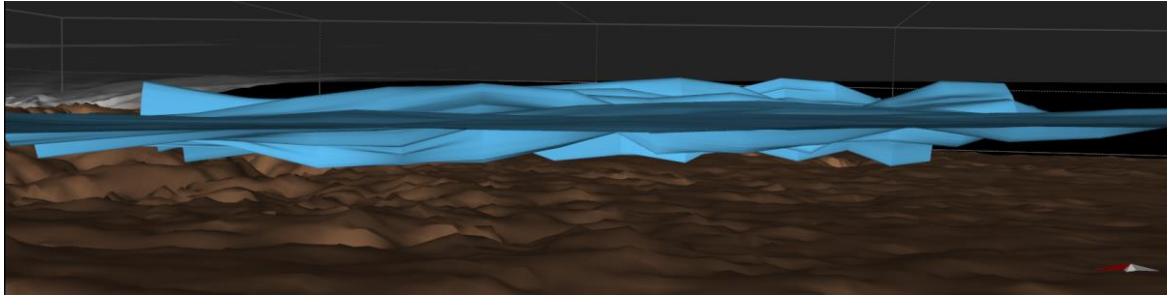
Figure 18. Surface gray_bottom, line of sight towards east, with underlying bedrock DEM and overlying ice surface DEM, illustrating the variability of the folds' height along flow.
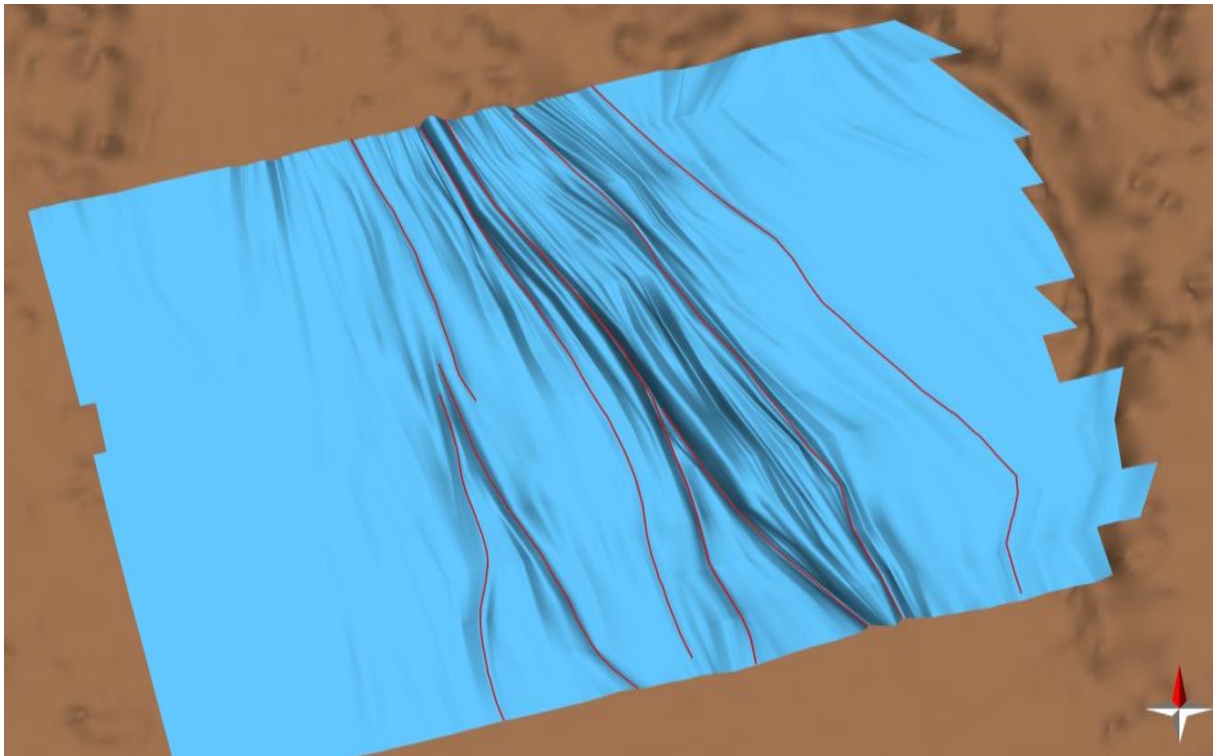
Figure 19. Bird's eye view of surface gray_bottom with underlying bedrock DEM. Red lines mark some distinct folds in order to visualize the changing across-flow width of fold areas. Width of image approximately 200 km.

The vertical position of the ice layers within the ice sheet varies strongly along the region (Figure 24 and Figure 26). At the rather undisturbed western margin, gray_bottom usually lies at depths of

50-60% of the total thickness (distance between ice surface and bedrock). In the central part, the ice layers are heavily disturbed and folding occurs. Here, gray_bottom's depth ranges from shallow 30% to deep 80% of total thickness. Generally speaking, the bedrock is rather horizontal in large parts of the area, and the ice surface is only slightly inclined, so the main reason for this great variability of the depth of gray_bottom lays in the internal deformations of the layers. Triple_mid shows similar variability in the vertical position. Also the thickness of distinct ice layers is very variable: For example the distance between gray_bottom and triple_mid ranges from less than 20 meters to about 400 meters within section_H12, where the ice has an average thickness of about 1600 meters. In rather undisturbed ice of this section, the distance is about 250 meters (Figure 20).
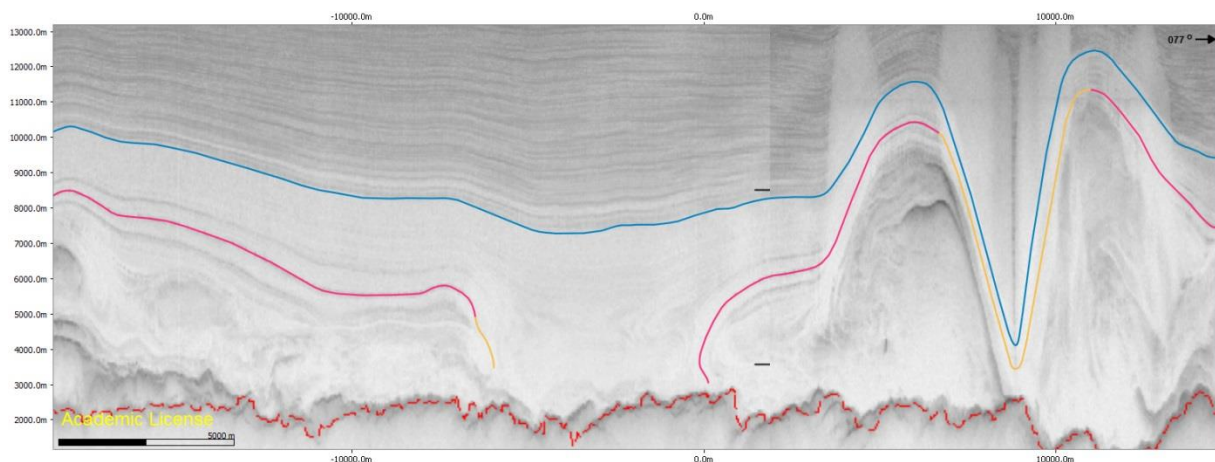
Figure 20. Detail of W-E striking Section H12 with horizons gray_bottom (blue) and triple_mid (magenta and orange), illustrating the high variability of layer thickness. Width of image approximately 33 km.

Generally, the amount of folding increases downwards within the ice. The upper third of the ice column is mostly unfolded or just gently folded. Below that (e.g. horizon gray_bottom), there are mainly upright or slightly inclined folds. At the margins of the belt, the folds tend to be more asymmetric and are often gently inclined towards the belt's center. Within triple_mid however, there are more often inclined or even recumbent folds. (Figure 24, Figure 26 and Figure 27)

The amplitudes of the folds become greater with increasing depth. In the upper layers, only gentle folding occurs, but within horizon triple_mid, amplitudes vary from less than 5 meters to about 450 meters, whereby all ranges occur in relatively small distance to each other. The wavelength of the folds varies as well, ranging from some hundreds of meters to about eight kilometers. Towards the glacier's outlet, the folds' wavelengths generally decrease.

While gray_bottom is a continuous surface of one reliability type only, triple_mid has surfaces of high reliability (created from horizons of high and medium quality), depicted in magenta and surfaces of low reliability (created from at least one horizon of low quality), depicted in orange (Figure 17b).

Additional, alternative suggestions for the position and shape of triple_mid have been added in two places (depicted in purple), where a second solution seems possible as well (for more detail, see chapter 6.3 – Reliability of the presented model and limits of the applied modeling techniques from page 37). In some places, no surface triple_mid has been created, because the layer apparently is not present, despite good quality of the radar imagery. The borders of these zones are mostly marked by recumbent or folds and/or lie near the bedrock (Figure 24 and Figure 26).

As the used radar imagery has a vertical exaggeration by factor ten, all horizons and surfaces created from them are also exaggerated by this factor. This should be kept in mind while evaluating the structures that are visible in the 3D model. However, the main shape and features of the fold belt are also clearly visible when the exaggeration is removed (Figure 21 and Figure 25).
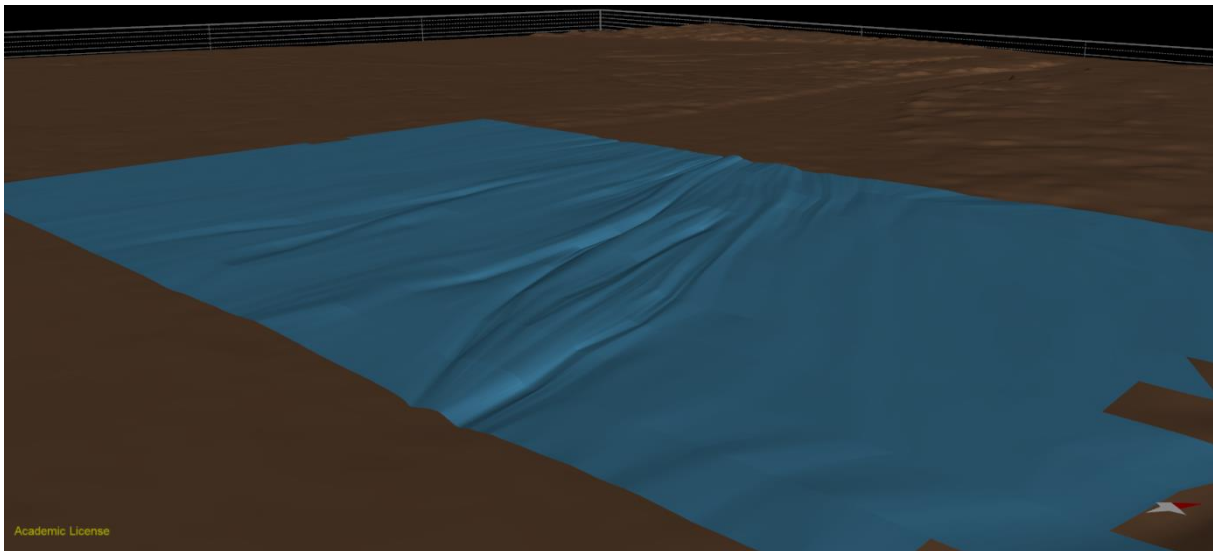
Figure 21. Surface gray_bottom with underlying bedrock, depicted without exaggeration. Line of sight is towards the northeast. The fold structures are clearly visible.

Additionally to the two ice layers that were visualized along the entire region, there is a third set of lines and surfaces named **strucs_mix**. It contains several ice layers below triple_mid and was picked where distinct eye-catching structures occur, to visualize the relatively small-scale deformations that can be seen especially in the lower layers of the ice sheet. While layers above triple_mid and gray_bottom tend to run very similar to them, only with smaller fold amplitudes, the structures formed in the layers underneath triple_mid are more complicated. The picked lines provide a good impression of the complex deformation these ice layers undergo and of their spatial development. Quite often recumbent and even diving folds can be observed (Figure 24, Figure 26 and Figure 27). In some sections encircled layers forming "eye"-like structures can be found (Figure 26).
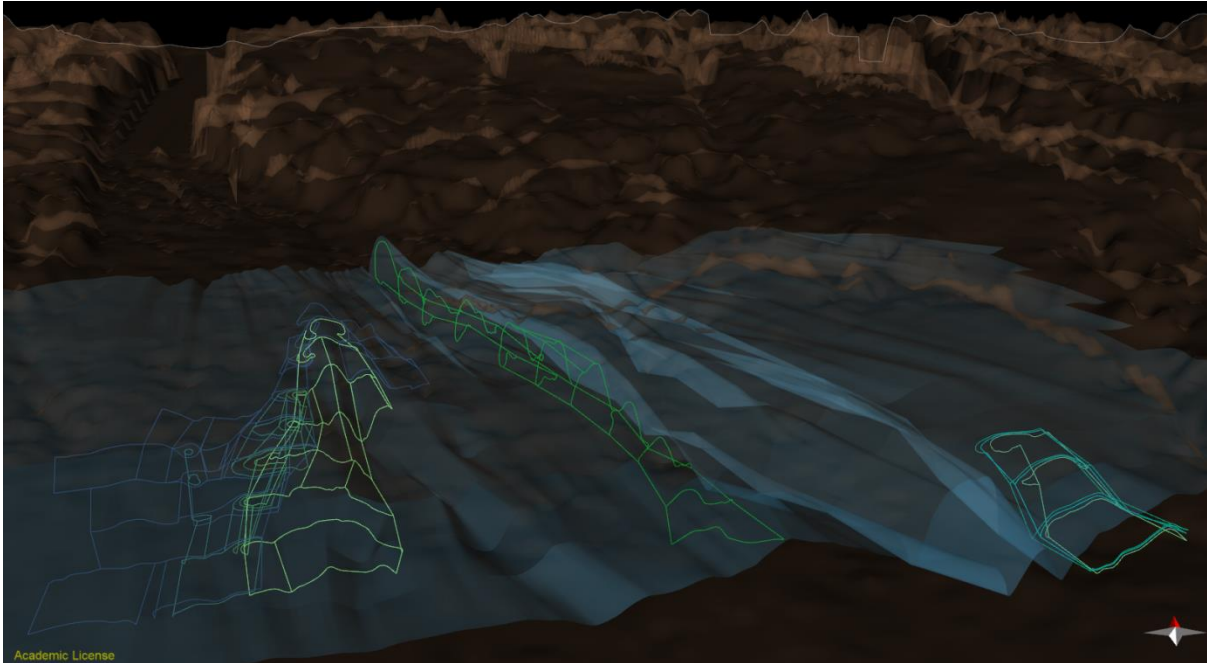
Figure 22. Surfaces created from layers of strucs_mix, depicted as surface boundaries in several shades of green. Underneath lying bedrock is depicted in brown color, overlying surface gray_bottom is depicted transparent and blue for orientation purposes. Line of sight is towards the north. Note the three regions discussed in the text.

It was rarely possible to identify matching ice layers in parallel running sections for certain, so only some surfaces were created from the lines of strucs_mix. Connected surfaces of the same color shade represent one specific ice layer. The surfaces are limited to small parts of the area, because the ice layers could not be identified elsewhere. If a surface of strucs_mix does not continue, it does not mean the ice layer does not occur elsewhere. Surfaces from strucs_mix were created in three regions (Figure 22 and Figure 27):

a)   A surface connecting a prominent horizon that lies inside the relatively tight anticline in the middle of the area. It appears very dark in the radar images and hence can be followed relative reliable along 11 sections. The shape of this surface resembles the shape of triple_mid and gray_bottom above it, but the amplitude of the fold is bigger and the fold limbs are steeper. Its amplitude increases and its wavelength decreases along flow direction. At the northernmost point of the area, his layer lies three times as high over bedrock at it would lie within undisturbed ice: 900 meters above bedrock instead of 300 meters, with an ice thickness of 1500 meters.

b)   Surfaces of layers within a fold system in the western part of the area. Because of the relatively high quality of the images and moderate variability between the sections, it was possible to match the lines of several ice layers and create surfaces from them to

visualize the inner structure of the folds. The large-scale anticlinal shape of the upper

layers can also be found here, but the folding gets tighter in the core and also contains

minor folds. Some ice layers even show recumbent and diving folds. Two encircled

layers forming "eye"-shaped structures could be identified in several sections (Figure

26). The surfaces produced from these lines form a long tubular shape, which gets

narrower along flow direction (Figure 23 and Figure 26). It is located relatively near to

the bedrock. This tubular structure, along with the prominent "eye"-shaped structures

resembles the appearance known from sheath folds.

c)   In the south eastern part of the area, a couple of surfaces could be created due to the

same reasons mentioned in b). However, only three matching ice layers between four

sections were identified. In this region, another example for near-cylindrical, partly

recumbent or diving folds can be found.

The vertical distribution of fold types can be summarized as follows: In the upper part of the ice

sheet, no folding is observed. Below that, near-cylindrical, mostly symmetric folds can be observed.

In the lowermost part, recumbent, diving and even sheath folds are possible.
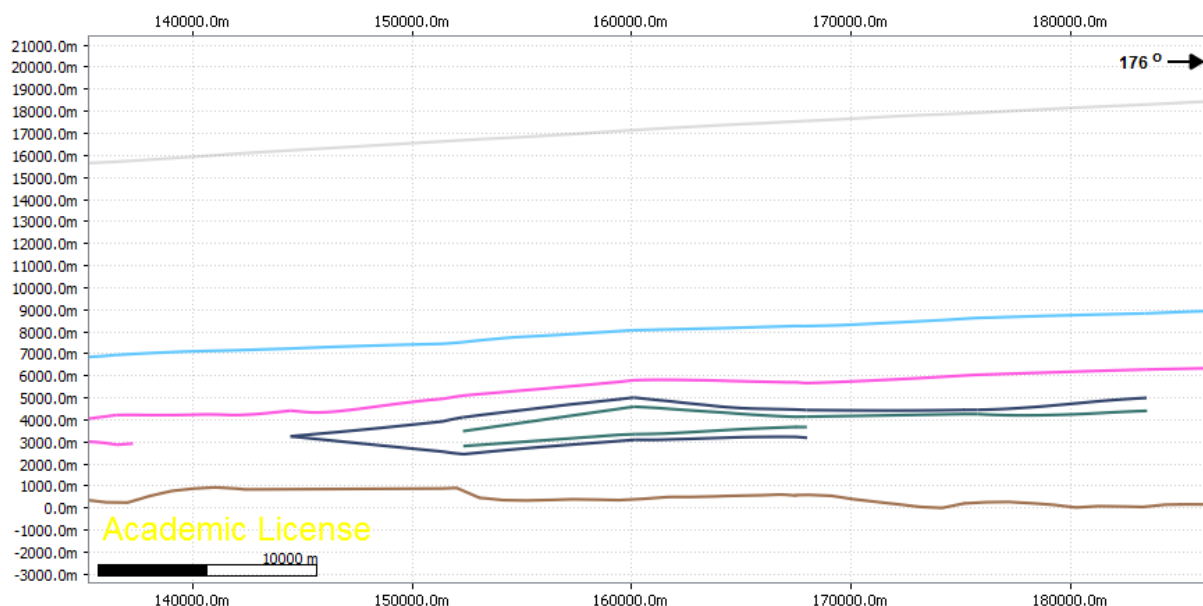
Figure 23. N-S striking cross section of the tubular, sheath-like fold structure in the western part of the modeled region. Note the exaggeration by ten.
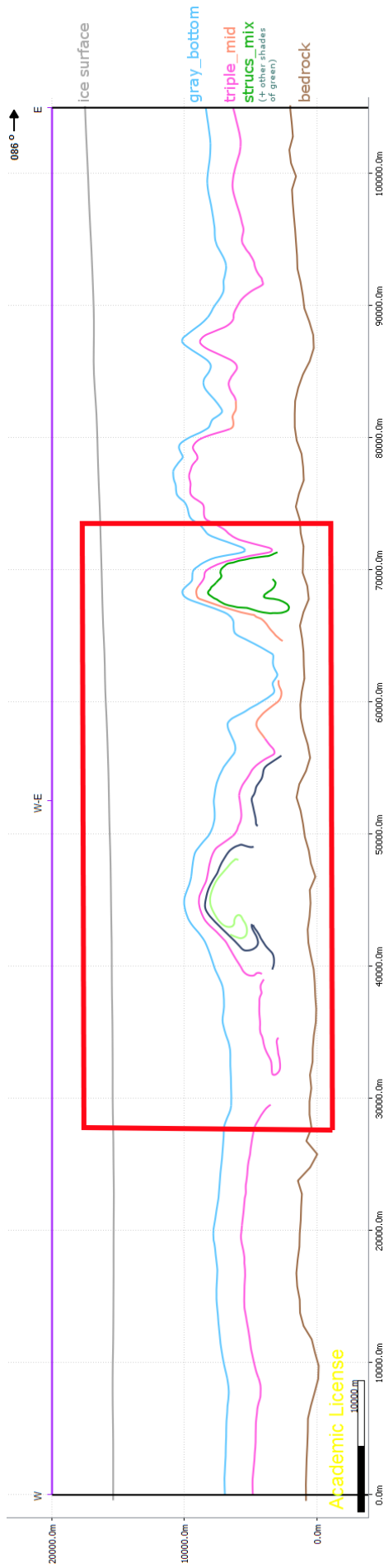
Figure 24. Cross section through the northern part of the created model, WE striking, showing the ice surface (gray), the horizons gray_bottom (blue) and triple_mid (magenta and orange), several structures of strucs_mix (several shades of green) and the bedrock (brown). Exaggerated by 10. Red box marks the region depicted in Figure 25. Note the recumbent and diving folds within triple_mid and strucs_mix and the variability of the vertical position of the layers.
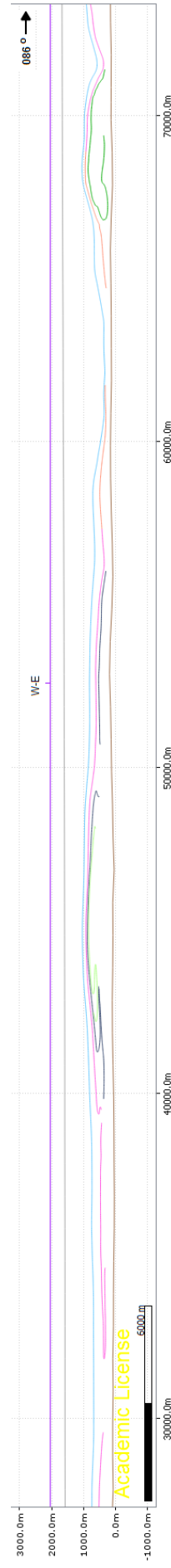
Figure 25. Cross section of the region marked by a red box in Figure 24, but without exaggeration.
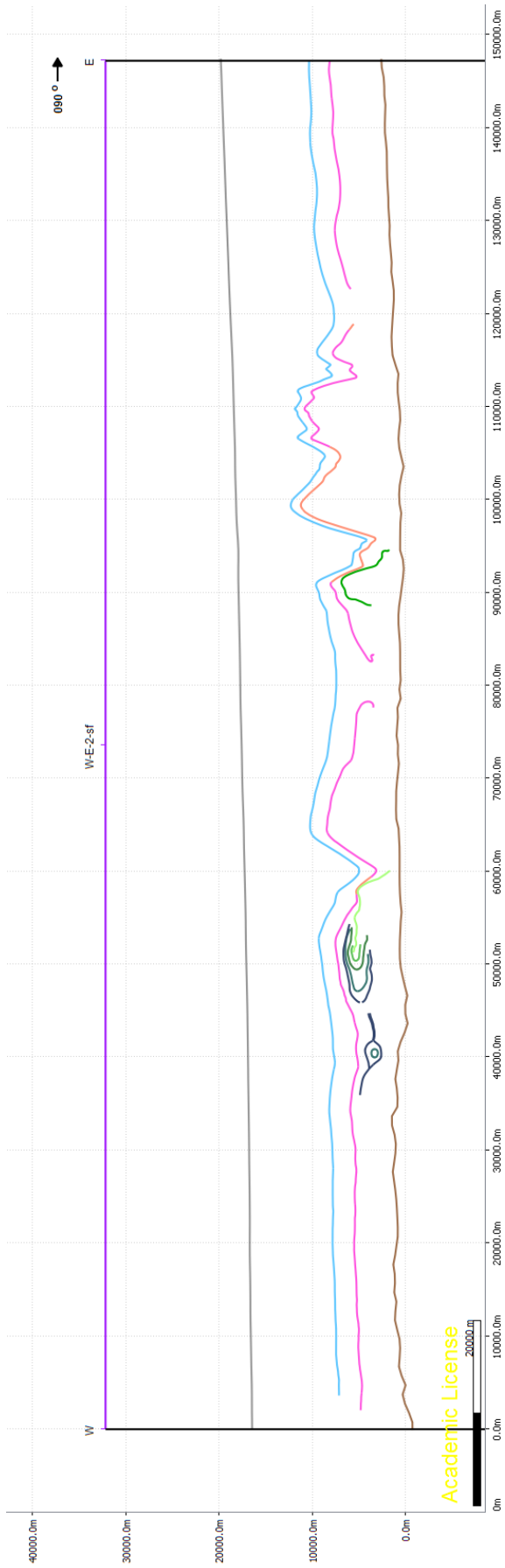
Figure 26. Cross section through the central part of the created model, WE striking. Shown surfaces see Figure 24. Exaggerated by 10. Note the "eye"-shaped structure in the western part, indicating a sheath fold. See text for more information.
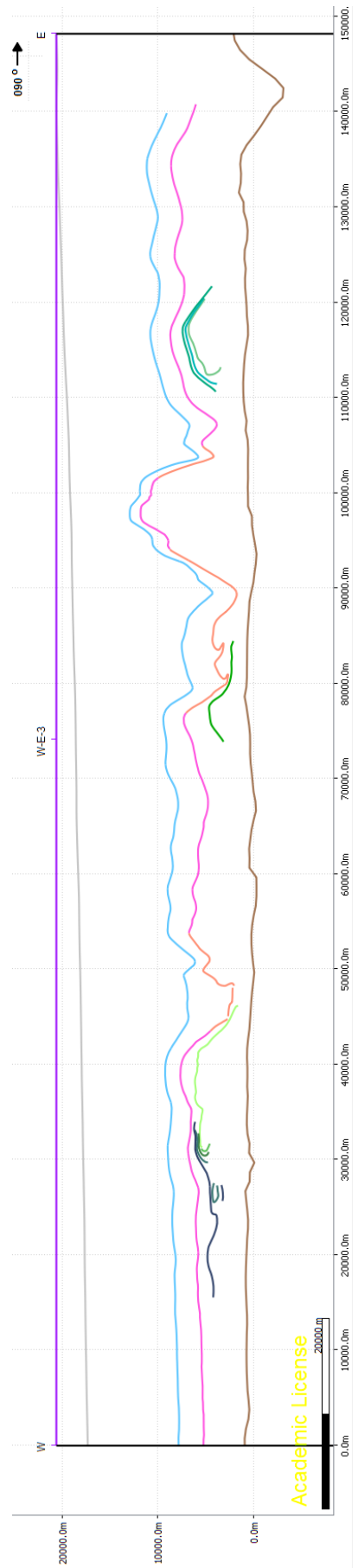
Figure 27. Cross section through the southern part of the created model, WE striking. Shown surfaces see Figure 24. Exaggerated by 10. All three regions where surfaces were created from strucs_mix occur in this cross section. See text for more information.

6   Discussion

6.1   The fold belt within the ice layers of the Petermann catchment

The observed fold structures have conspicuous properties: They strike along flow direction of the glacier. The folds have higher amplitudes and steepness in the middle of the funnel-shaped catchment area, and at the borders they tend to be vergent towards the center of the catchment. The tapering fold areas and the decreasing wave lengths also suit these observations. All these indications make it highly probable that the folding of the ice layers is linked to the compression the ice undergoes while entering the funnel-shaped outlet of the glacier area. As Wilson (1967) notes, it is possible to get a fold-bundle in a compressive regime, in whose center the most pronounced folds are present, because the forces are maximal, while at the margins the folds fade away. An often drawn comparison is to imagine a tablecloth being pushed together, which causes a series of antiforms and synforms to develop.

In the setting of Petermann Glacier, it is important to consider the velocity of the ice moving towards the outlet of the glacier, too. As a map of the velocity magnitudes of the ice has been added to the model, it is possible to see that the fold belt is most pronounced where velocities are high (Figure 28b). The increasing ice velocities towards the outlet of the glacier produce tensional stress, as north western ice layers – which are closer to the outlet – move faster than south eastern ice layers. Combining the compressional forces that occur through the funnel shape of the area with the tensional forces through the acceleration along flow, one can assume a pure shear dominated deformation when considering the xy-plane (viewed from above, Figure 28a).

The ice velocities might also have an impact on the compressional forces, which are result of the funnel-shaped outlet. For this thesis, it was only possible to display the magnitude of ice velocities. To gain an insight on the direction of the velocities, it would be an idea to display the velocities as vectors over the area. By looking at the direction of the vectors especially at the margins of the funnel, it would be possible to find out if also the ice velocities indicate a compressional force across flow direction.
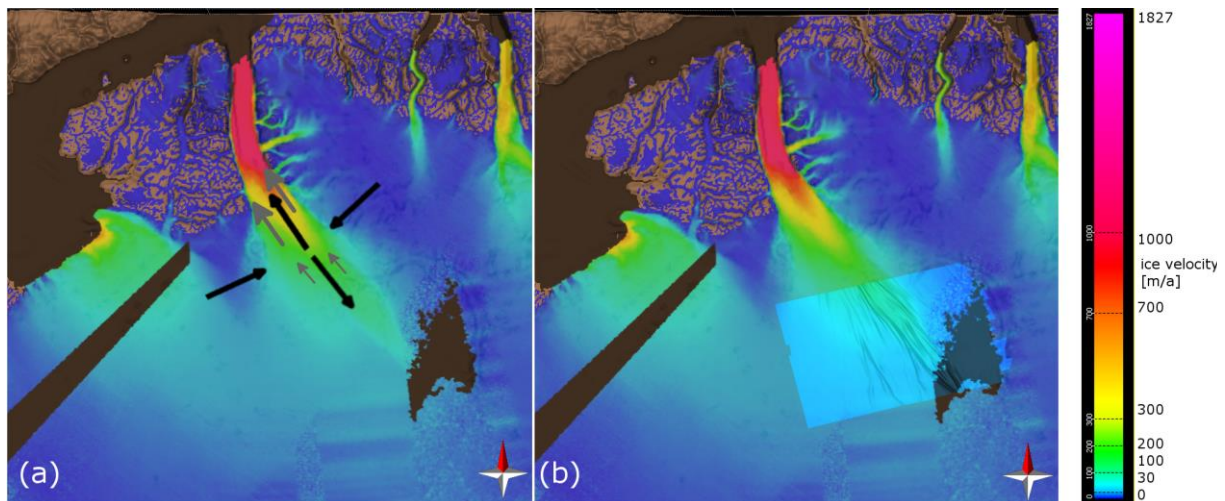
Figure 28. **(a)** Bedrock (brown) and ice velocities of the Petermann catchment. Black arrows indicate the tensile and compressive stress; gray arrows indicate the increasing ice velocity within flow direction, which leads to the extensional forces. **(b)** Bedrock (brown) and ice velocities with horizon gray_bottom (blue)

The folding does not reflect the underlying bedrock, and also further upstream there are no significant bumps or mounds in the bedrock that could indicate that the folds were created there and transported downstream afterwards.

The large-scale folding of the ice layers clearly is a result of compressional and tensional stresses acting within the catchment of Petermann Glacier. Refreezing melt water (Bell et al., 2014) or slippery ice patches (Wolovick et al., 2014) might have an additional influence on the shape of the folds and the particular high amplitudes, but primary processes like the described tectonic forces are much more likely to create such fold belts like the observed. NEEM community members (2013) held rheology contrasts within the ice responsible for the creation of the folds. However, the high anisotropy even of rheological homogenous ice can lead to folding (Thorsteinsson, 2000). Furthermore, a rheology contrast between Eemian and glacial ice that leads to the creation of folds in the latter does not explain the different types of folds that can be observed within different ice depths. This topic will be considered in the following sub-chapter.

6.2   Vertical distribution of specific fold structures within the ice

It is conspicuous that the amount of folding increases vertically towards the base of the ice sheet, as well as the diversity of shapes the folds assume does. The upper ice layers are not or only gently folded, then the amplitude increases, forming cylindrical, mostly symmetric folds, and even more below, complicated structures occur, such as recumbent folds, diving folds and sheath folds. Recumbent folds within triple_mid are associated with the widening of a fold area and occur below synclines of overlying ice. In most cases it is not possible to follow the ice layer beyond the recumbent fold, as if the horizon has been "torn apart". As these recumbent folds often occur in

widened areas, this could be a sign for local tensile strain (extensional forces). Most likely the horizon is still present, but much harder to spot in the radar images because it has become very thin. It has to be differentiated between such "torn"-like, downward pointing, recumbent folds that occur mostly in local fold troughs, and diving folds, which tend to lie within local fold saddles. They rather seem to be the result of shortening than of extension.

Recumbent, torn-looking folds often are located near the bedrock (less than 200 meters above it) and lie within (first-order) synclinoria, so another possible explanation could be that interactions with the bedrock during the flow lead to such structures. However, the amount of recumbent folds does rather seem to decrease towards the outlet of the glacier. That fact rather favors the connection to tensile forces, as compression and shortening probably increase towards the outlet.

In the western part of the model region, a sheath fold's surface has been created from clearly "eye"-shaped ice layer cross sections. The sheath fold is very flat, considering the model's exaggeration by a factor of ten. Its fold axis lies nearly parallel to the fold limbs, indicating that a large shear strain did cause the fold. In order to estimate the amount of shear strain, it was tried to "re-shear" a screenshot of the sheath fold's cross section using a picture editing software. However, no useful results were gathered by this attempt, because the unfolding of the sheath fold happened extremely slowly. At a shear strain of 5, the fold axis had barely rotated, but the screenshot was already so deformed that little of the original layering could be recognized. One can infer from this that the shear strain that was needed to create this sheath fold was very high.
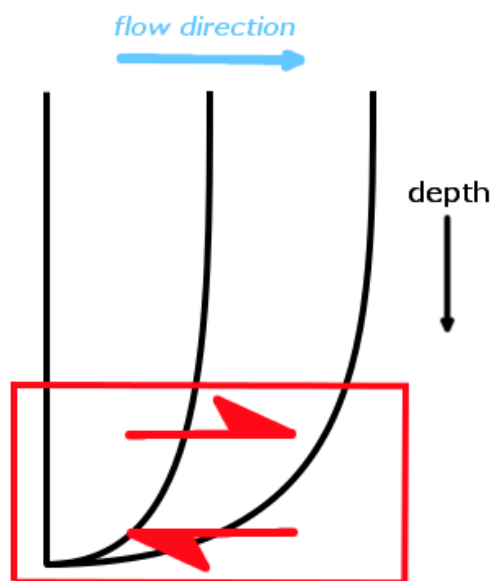
Figure 29. Schematic sketch that illustrates how a vertical line within the ice sheet gets deformed along flow direction. The red box indicates the dominance of simple shear in the lower part of the ice.

The vertical distribution of the occurring fold structures from ice surface to bedrock (no folding – cylindrical open folds – recumbent and diving folds – sheath folds) can be associated with increasing shear stress affecting the ice layers. This fits the assumption that from a certain minimum depth on, the ice's horizontal flow velocity decreases exponentially with increasing depth, presuming that the ice is frozen to the bedrock (Dansgaard and Johnsen, 1969). This vertical difference in ice velocity leads to a regime of simple shear strain, where shearing increases with increasing depth (Figure 29).

With such strong shearing forces active, this is an explanation for the occurrence of sheath folds near to the bedrock, where the difference in ice velocity is maximal and simple shear is the dominant process. In the upper part of the ice, the velocities are more homogenous, so simple shear is not the main type of deformation here, but rather pure shear due to extensional forces along flow because of the increasing ice velocity towards the outlet of the glacier, and compressional forces perpendicular to it, because of the constriction through the funnel shape of the glacier. The recumbent and diving folds occurring in intermediate depths could be explained by an intermediate regime between dominating pure shear at the top and simple shear at the bottom of the ice block.

It has to be considered that the deeper the ice layers, the more upstream they have been accumulated. Thus, their deformation could have taken place before they moved into the Petermann catchment and does not have to be connected with Petermann's topography and the local ice velocities. The vertical distribution of ice velocities along the ice column applies in the entire ice sheet, not only in the region of outlet glaciers. However, an aim of future studies could be to investigate differences regarding occurrence and distribution of sheath folds within glacier catchments compared to the interior of the Greenland ice sheet. "Eye"-like structures that could be sheath folds can also be found in other regions than the catchment of Petermann Glacier (Figure 30).
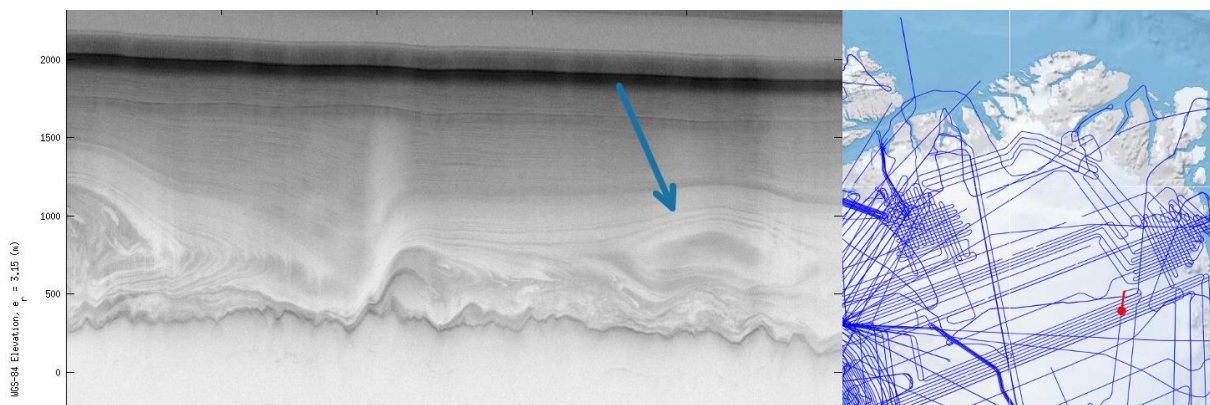
Figure 30. An example for the possible occurrence of sheath folds in other regions than the study area. This "eye"-like fold shape (indicated by blue arrow) lies in the Northeast Greenland Ice Stream (NEGIS), the position is marked in the image on the right.

Another question certainly is, whether large folding structures do also occur in other glacier's catchment areas than that of Petermann Glacier. While browsing CReSIS' radar images of Greenland, several other glaciers have been discovered where large folding occurs, independent from the bedrock: Upernavik Glacier in West Greenland and Nioghalvfjerdsfjorden Glacier at the north western edge of Greenland (Figure 31). However, there are only few glacier outlet regions where images with a quality as high as Petermann's images are provided, which hinders the search for comparable regions.
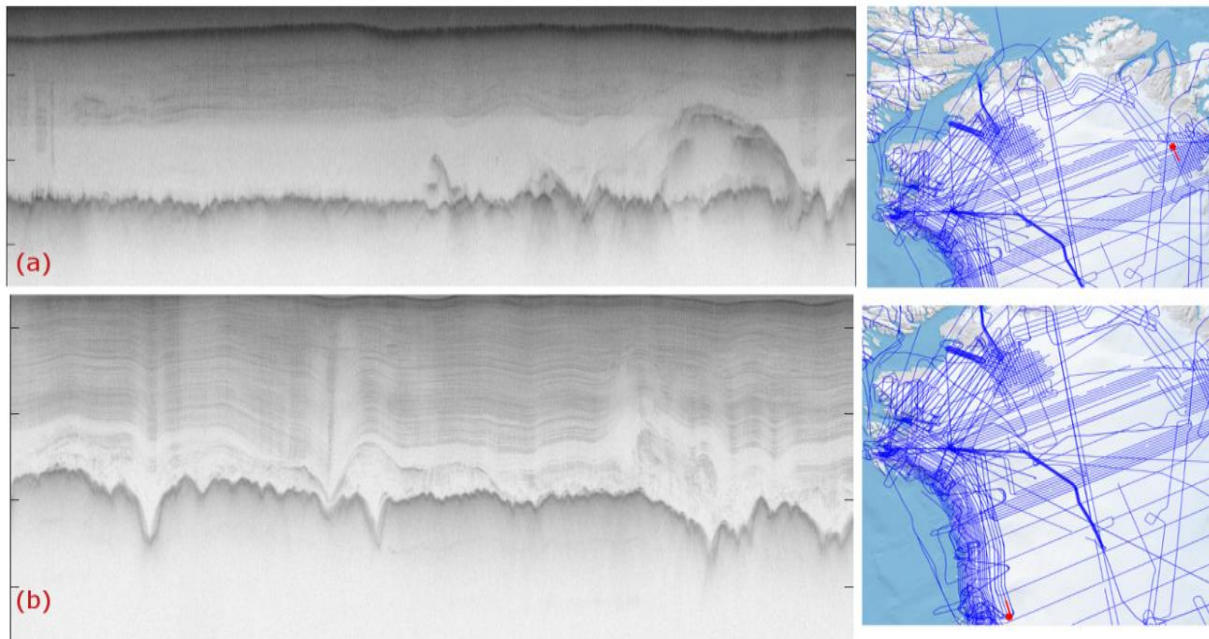
Figure 31. RDS frames no. **(a)** 20100330_07_013 (Nioghalvfjerdsfjorden Glacier) and **(b)** 20140509_01_046 (Upernavik Glacier), illustrating that folding of internal ice layers also occurs in other regions. The maps on the right show the position of the radar images, marked in red. Width of radar images approx. 50 km.

6.3   Reliability of the presented model and limits of the applied modeling techniques

A main question of this project was to find out, whether or not it is possible to create a 3D model from the radar images of ice sheets, using a geological modelling program such as MOVE. In this sub-chapter, I discuss the reliability of the model I created, the problems within the modeling process and further work that could be done to improve the modeling procedure and its results.

An obvious limiting factor within the model's quality is the quality of the radar imagery used. Within the considered region, only the images from 2011's flight missions were sharp enough to distinguish internal layers and smaller structures. From images with a quality as low as those of 2010 (in our region), it is not possible to create such a model. Another problem is the "white zones" occurring within the images, where no proper radar signal returned from the ice layers. This happens

if the ice layers are too steep and the reflected signal gets scattered. It was a bit tricky to pick the horizons in these zones, but with enhanced image contrast and by regarding the adjacent zones where proper signals were present, it was possible to pick the horizons on positions that are quite reliable. As the images are vertically exaggerated by ten, and there always are uncertainties when manually picking lines, one has to assume anyway that the vertical position of the picked lines contains inaccuracies up to some tens of meters. However, in a region of this size, and within a model that's main purpose is to have a qualitative look at the relative position of ice layers, such errors are tolerable.

To distinguish between areas of high and of lower reliability of the model, different colors were used for the creation of the lines and surfaces. This also ensures that it is possible to classify how reliable these areas are.

A major difficulty lies within the spacing of the radar profiles. Although the catchment of Petermann Glacier is one of the regions of Greenland with the densest radar grid, the spacing of two parallel sections (7 to 9 km) still is much bigger than the wavelength of many of the folds occurring in this region's ice layers. This produces the problem that as it is only possible to see the situation within the profiles, we do not know what happens in between them. Whatever modeling technique is chosen – in between the picked lines the surfaces always just get interpolated. Structures that are smaller than the resolution of the grid thus cannot be depicted in the model (Figure 32). Hence, it has to be kept in mind that the surfaces created for the model are only a interpretation of the available lines. This means that large structures that stretch over several sections are much more reliable than smaller, minor structures created by the model.
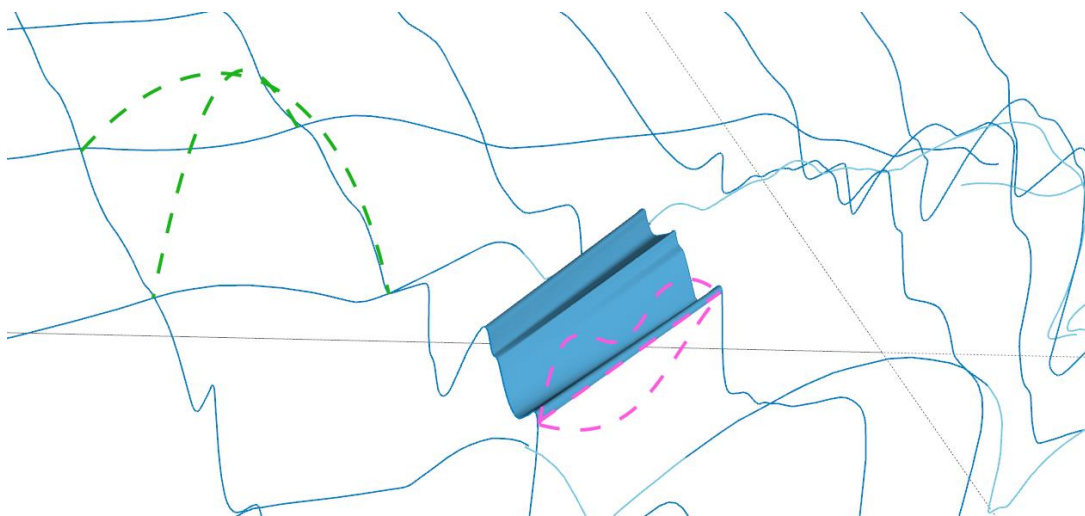
Figure 32. Lines and surfaces of gray_bottom, illustrating the problem with the resolution of the grid. The surfaces get created by interpolation, straight lines are drawn between points of adjacent sections. The straight dashed purple line is the border of the displayed surface, but it rather could run like one of the other two dashed purple lines. The green dashed lines illustrate that – though not likely – it would not be known if there were a big anticline in the middle of the picked lines. Line of sight is towards the East.

This could be one of the reasons that only one proper sheath fold could be depicted within the model. Typical "eye"-like structures can be found in other places of the region, too, but never in two or more parallel sections. To follow such small structures over several sections, the sheath fold has to be very long and the adjacent ice layers must not be too disturbed or folded, as otherwise it will be difficult to recognize matching horizons reliably.

For the creation of the surface, the "Linear" method was used. It was also considered to use the "Delaunay Triangulation" method, which creates little triangles between lines, taking all lines into account, while for the "Linear" method, only parallel lines can be used. However, this method turned not out to be suitable, because it creates much bigger triangles near the intersection points of lines than in between them. It is also not able to consider the most likable course of the horizons and will rather create many single folds than a long fold belt. Because the horizontal (WSW-ENE striking) lines have a higher quality than most of the vertical (NNW-SSE striking) lines, and because they show much more variability and folds with small wavelengths, it was considered to be the best to create the surfaces from them. Nevertheless, the vertical sections were essential to get an impression of the folds' course and played an important role when deciding which points of the horizons were connected to surfaces. Hence, a grid of perpendicular sections can be used for the creation of models with much more reliability than only parallel sections, because they allow a much better impression of the three-dimensional shape of the horizons.
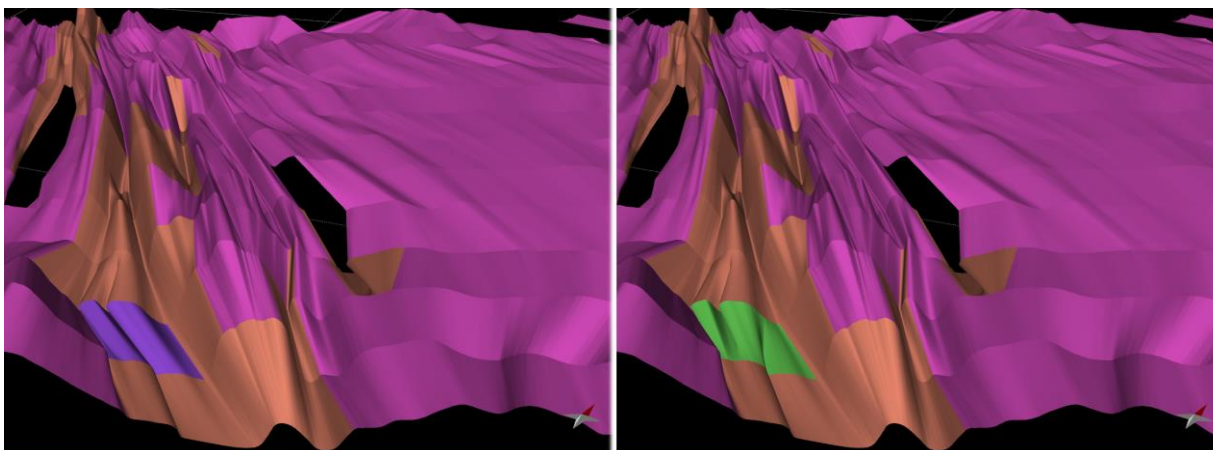
Figure 33. Alternative surfaces created for horizon triple_mid, highlighted in purple and green, respectively.

In order to create a surface, the lines had to be cut to pieces, of which the end points certainly match, because they will get connected when creating a surface. Sensible end points are e.g. hinge points of large folds. When two neighboring sections differ very much because of small-scale folding,

it sometimes was hard to determine points of the horizons that should be connected. For the creation of surface triple_mid, which contains several recumbent folds, I created two alternative solutions in several ambiguous regions, which both can be displayed in the model (Figure 33).

While the large fold-belt structures can really well be observed in the presented model, for the more detailed investigation of smaller structures the grid of sections is not dense enough. But the existing model can be used to identify regions of particular interest, in order to determine further investigations. Another flight mission with much smaller spacing (e.g. 1 km) within a small region would be suitable to gather further knowledge about the shape of smaller internal structures, such as recumbent, diving or sheath folds.

If a smoother surface model created from the existing sections was desired, it would be possible to create intermediate lines between every set of two parallel horizontal lines. In order to do so, one could convert the existing surfaces to points and connect the points in the middle to a line lying parallel to the other lines. By intersecting this line with the existing vertical lines and fitting it to their shape, intermediate lines could be produced that match the shape of the vertical lines better than the current surfaces do. Afterwards, smoother surfaces could be created from the old and the new lines. However, this process could only help to smooth the surface and to match its shape to the course of the vertical lines. In between the lines, the data density does not increase and the surface's shape still depends on interpolation.

7 Conclusion

The aim of this bachelor project was to investigate the feasibility of creating a three-dimensional model of internal layers of polar ice sheets using geological modeling software and radar imagery. This was done using the example of Petermann Glacier, Greenland. Furthermore, the internal structures of the ice and their geologic interpretation were a subject of this thesis.

It can be put to record that it is possible to create a reliable 3D visualization of internal layers of polar ice sheets, if the quality of the used radar images is high enough. Depending on the density and arrangement of the image grids, confidential large or even smaller geologic structures can be depicted in a 3D model. The creation of the surfaces out of picked lines always depends on interpolation; hence the shape of the developed surfaces should still always be questioned.

For the creation of the observed fold belt, basic geologic processes are responsible. The funnel-like shape of the glacier leads to compression. Combined with extensional stress, which occurs because of the increasing ice velocity in flow direction, a regime of pure shear strain is created. This leads to the evolution of cylindrical folds in intermediate depths. Below that, recumbent and diving folds occur. Because the ice velocity decreases with increasing depth, strong simple shear dominated stress occur in the lowermost parts of the ice sheet, leading to the genesis of sheath folds.

8 References

Alsop, G.I. and Carreras, J., 2007: The structural evolution of sheath folds: A case study from Cap de Creus. *Journal of Structural Geology* **29**, pp. 1915-1930. doi:10.1016/j.jsg.2007.09.010

Alsop, G.I. and Holdsworth, R.E., 2006: Sheath folds as discriminators of bulk strain type. *Journal of Structural Geology* **28**, pp. 1588-1606. doi:10.1016/j.jsg.2006.05.005

Alsop, G.I., Holdsworth, R.E., and McCaffrey, K.J.W., 2007: Scale invariant sheath folds in salt, sediments and shear zones. *Journal of Structural Geology* **29**, pp. 1585-1604. doi:10.1016/j.jsg.2007.07.012

Bamber, J.L., Griggs, J.A., Hurkmans, R.T.W.L., Dowdeswell, J.A., Gogineni, S.P., Howat, I., Mouginot, J., Paden, J., Palmer, S., Rignot, E., and Steinhage, D., 2013: A new bed elevation dataset for Greenland. *The Cryosphere* **7**, pp. 499-510. doi:10.5194/tc-7-499-2013

Bell, R.E., Tinto, K., Das, I., Wolovick, M., Chu, W., Creyts, T.T., Frearson, N., Abdi, A., and Paden, J.D., 2014: Deformation, warming and softening of Greenland's ice by refreezing meltwater. *Nature Geoscience* **7**, pp. 497–502. doi:10.1038/ngeo2179

Benn, D.I. and Evans, D.J.A., 2010: *Glaciers & Glaciation, 2nd edition*, Hodder Arnold Publication, London, 816 p.

Carreras, J., Druguet, E., and Griera, A., 2005: Shear zone-related folds. *Journal of Structural Geology* **27**, pp. 1229-1251. doi:10.1016/j.jsg.2004.08.004

Dansgaard, W. and Johnsen, S.J., 1969: A flow model and a time scale for the ice core from camp century, Greenland. *Journal of Glaciology* **8**, pp. 215-223.

Davis, G.H., Reynolds, S.J., and Kluth, C.F., 2011: *Structural Geology of Rocks and Regions, 3rd edition*, Wiley, Hoboken, 839 p.

Ez, V., 2000: When shearing is a cause of folding. *Earth-Science Reviews* **51**, pp. 155-172. doi:10.1016/S0012-8252(00)00020-9

Fujita, S., Matsuoka, T., Ishida, T., Matsuoka, K., and Mae, S, 2000: A summary of the complex dielectric permittivity of ice in the megahertz range and its applications for radar sounding of polar ice sheets. In Hondoh, T. (ed.), *Physics of Ice Core Records*, Hokkaido University Press, Sapporo, pp. 185-212

Gogineni, P., 2012: CReSIS RADAR DEPTH SOUNDER Data, Lawrence, Kansas, USA. Digital Media. http://data.cresis.ku.edu/

Goodsell, B., Hambrey, M.J., and Glasser, N.F., 2002: Formation of band ogives and associated structures at Bas Glacier d'Arolla, Valais, Switzerland. *Journal of Glaciology* **48**, pp. 287-300. doi: 10.3189/172756502781831494

Hudleston, P.J. and Treagus, S.H., 2010: Information from folds: A review. *Journal of Structural Geology* **32**, pp. 2042-2071. doi:10.1038/nature11789

Hvidberg, C.S., Svensson, A., and Buchardt, S.L., 2013: Dynamics of the Greenland Ice Sheets. In Elias, S. and Mock, C. (ed.), *Encyclopedia of Quaternary Sciences, 2nd Edition*, Elsevier, Oxford, pp. 439-447.

Joughin, I., Smith, B., Howat, I. and Scambos, T., 2010: *MEaSUREs Greenland Ice Velocity Map from InSAR Data.* Boulder, Colorado, USA: NASA DAAC at the National Snow and Ice Data Center. doi:10.5067/MEASURES/CRYOSPHERE/nsidc-0478.001

NEEM community members, 2013: Eemian interglacial reconstructed from a Greenland folded ice core. *Nature* **493**, pp. 489-494. doi:10.1038/nature11789

NEEM homepage: *The last interglacial and beyond: A northwest Greenland deep ice core drilling project.* Available online at http://neem.dk/neeminfo.pdf (access date: March 9th, 2015).

MacGregor, J. A., Fahnestock, M. A., Catania, G. A., Paden, J. D., Gogineni, S. P., Young, S. K., Rybarski, S. C., Mabrey, A. N., Wagman, B. M., and Morlighem, M., 2015: Radiostratigraphy and age structure of the Greenland Ice Sheet. *Journal of Geophysical Research: Earth Surface* **120**. doi:10.1002/2014JF003215

Morlighem, M., Rignot, E., Mouginot, J., Seroussi, H., and Larour, E., 2014: Deeply incised submarine glacial valleys beneath the Greenland ice sheet. *Nature Geoscience* **7**, pp. 418-422. doi:10.1038/ngeo2167

Ramsay, J.G. and Huber, M.I., 1987: *The techniques of modern structural geology, volume 2: Folds and Fractures*, Academic Press, London, 391 p.

Reuther, C.-D., 2012: *Grundlagen der Tektonik: Kräften und Spannungen der Erde auf der Spur*, Springer Spektrum, Berlin, 274 p.

Rignot, E. and Kanagaratnam, P., 2006: Changes in the Velocity Structure of the Greenland Ice Sheet. *Science* **311**, pp. 986-990. doi:10.1126/science.1121381

Rignot, E., Box, J., Burgess, E. and Hanna, E., 2008: Mass balance of the Greenland ice sheet from 1958 to 2007. *Geophysical Research Letters* **35**, L20502. doi:10.1029/2008GL035417

Rodríguez-Morales, F., Gogineni, S., Leuschen, C.J., Paden, J.D., Li, J., Lewis, C.C., Panzer, B., Gomez-García Alvestegui, D., Patel, A., Byers, K., Crowe, R., Player, K., Hale, R.D., Arnold, E.J., Smith, L., Gifford, C.M., Braaten, D., and Panton, C., 2014: Advanced Multifrequency Radar Instrumentation for Polar Research. *IEEE Transactions on Geoscience and Remote Sensing* **52**, pp. 2824-2842. doi:10.1109/TGRS.2013.2266415

Thomas, R.H., 2001: Program for Arctic Regional Climate Assessment (PARCA): Goals, key findings, and future directions. *Journal of Geophysical Research* **106**, pp. 3691-33705. doi:10.1029/2001JD900042

Thorsteinsson, T., 2000: Anisotropy of ice I_h: *Development of fabric and effects of anisotropy on deformation.* University of Washington.

Wilson, G., 1967: The geometry of cylindrical and conical folds. *Proceedings of the Geologists Association* **78**, pp. 179-209. doi: 10.1016/S0016-7878(67)80043-9

Wolovick, M.J., Creyts, T.T., Buck, W.R., and Bell, R.E., 2014: Traveling slippery patches produce thickness-scale folds in ice sheets. *Geophysical Research Letters* **41**, pp. 8895-8901*,* doi:10.1002/2014GL062248

9 Appendix

9.1 Detailed explanation about the creation of the 3D-model in MOVE

In this step-by-step instruction I will explain in detail how the 3D-model was created in the 3D modeling program MOVE by Midland Valley. The explanation is based on **MOVE 2013.1**, but the creation of the model should also be possible with older or newer versions, partly with different names of buttons and settings, though.

Most tools within MOVE are organized within *Panels* (Model Building, Data & Analysis, View, Modules), which are sub-divided into several *Segments*, which contain the *Tools*. When it is explained in the following instructions how to navigate to a specific tool, this gets abbreviated in the following style: **Panel → Segment → Tool**.

For many operations, it is useful to keep the **Model Browser** open, where it is possible to browse through all objects the model contains. To open the Model Browser, click the button next to the arrow-buttons in the menu bar (Figure 34). As some operations can only (or better) be done within a specific view mode, it is sometimes needed to switch between **3D** and **2D**. To do so, choose the **View** panel, segment **Create Views** and the button of the desired view (**3D View** or **2D Map**). As the model is exaggerated by the factor ten, it can be useful to know how to look at it without the exaggeration. In the toolbar below the view window, there is an input box for the exaggeration. Reduce the standard of "1,00" to "0,10" to remove the exaggeration.
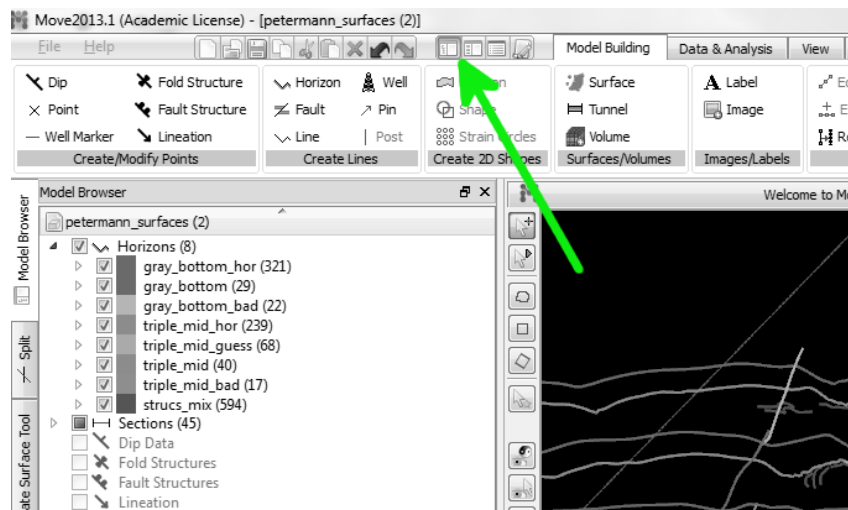
Figure 34. For opening the Model Browser, click that button.

9.1.1   *Importing and adjusting the radar depth sounder images*

Regarding the preparation and cutting of the images, please see chapter 4.2 – Handling of images and data from page 15 on.

Click **File** and **Insert…** for the import of an image. From the file format list on the bottom right of the opened window, choose **GIS Data – Raster Files** and navigate to the storage location of the image files. Choose the file you want to import and click **Open**. If the image were cut beforehand as I described in chapter 4.2, nothing has to be done in the next window and you can click **Next**. Otherwise place the check mark on **Import Sub Region** and adjust the limits of the appearing red box to the right limits (then click **Next** as well). Choose **Vertical extents** in the next window, keep the check box **Create Section With Image** ticked and click **Next**. Type the correct position coordinates for the top left and bottom right corner of the image into the boxes, using the coordinates in Bamber projection, which can also be found in this appendix under 9.2 – Overview of the images used on page 49. For the z-values, any values with a difference of 35.000 m can be used (e.g. 20.000 for top left and -15.000 for bottom right), because the images have to get adjusted (to each other and to the DEMs) manually anyway. Click **Load** to finish the import of the image. Now, you have a new **Section** containing a **Trace Line**, two vertical **Posts** and the **Image**. You can browse through all your elements in the **Model Browser**.

For the vertical adjustment of the images relative to each other, use one of the images as fixed point and adjust the other images successively to an adjacent image that is the fixed point or has already been adjusted. To do this, it is best to display only the two sections in question by removing the checkmarks next to all other sections in the Model Browser. Use the zoom to focus on the intersection line of the two sections. Double-click on the section you want to adjust in the Model Browser to open it in **Section View**. Now right-click on the section in the Model Browser and choose **Select all**. Now choose **Model Building → Data Modification → Transform**. Ensure that **Selected objects** is picked. From the list **Transformation Type**, choose **Translate**. In the box above, all four objects of the section (trace line, two posts, and image) should appear, because you want to move the entire section, not only the image. Type the desired amount of offset into the box next to **Vertical**, with positive values for an upward movement and negative values for downward. To find out how much offset is roughly required, you can click on a prominent horizon in each of the two images (near the intersection line). In the bottom left of MOVE's interface, the coordinates of the clicked point is displayed. The difference between the z-values of the two positions is the required offset. For the fine-tuning of the adjustment, it is necessary to have a close look at the intersection of the two images, maybe from changing sides, and to apply several smaller adjustments (in steps of 50

m or so) to get the best fitting. Just make sure to use the Transform tool only with Section View open, because it will not work otherwise.

9.1.2 Picking the horizons

It is sensible to organize the lines in horizons within a stratigraphy. For doing this, choose **Data & Analysis → Editors → Stratigraphy**. Here you can determine the horizons used for the model. Click on the green-white **"plus"-Symbol (+)** to add a new horizon. Double-click the cell in the row "Horizon" to determine the name of the horizon (e.g. gray_bottom) and double-click the cell in the row "Colour" to choose a color in which the lines of the particular horizon shall be displayed.

To pick the horizons of a section, open it in **Section View** (by double-clicking on its name in the Model Browser). Choose **Model Building → Create Lines → Horizon** to open the tool for the creation of horizons. Select the horizon you want to pick from the list **Horizon Assignment**, where all horizons are listed that were defined in the stratigraphy before. As **Creation Mode** choose **No Snap**. Then create the horizon starting on either side of the radar image. A line consists of several straight lines of which the starting and end points are determined by clicking on a place in the image, creating nodes of the horizon. The more nodes you produce, the smoother the horizon gets. Right-click to finish the creation of a line.

To edit the line afterwards, mark the line by clicking on it while having the Model Browser open, and choose **Model Building → Data Modification → Edit**. Now the nodes of the line are displayed and you can change their position by drag-and-drop and add new nodes by clicking on the line between two existing nodes.

9.1.3 Creating the surfaces from the horizons

To create piercing points a section's horizons through a section perpendicular to it, ensure that all horizons and sections are visible. Then right-click the section's name in the Model Browser and choose **Collect All Intersections (Active View)**. Now it can be found out if the horizons match. If not, it can be decided which horizon is more reliable and the other can be adjusted.

For the creation of the surfaces, re-organize the horizons of adjacent horizontal sections within one long horizontal section. To do so, select all objects that belong to the adjacent sections (e.g. H_04-1, H_04-2, H_04-3 and H_04-4), right-click into the view window and choose **Fit Straight Section Trace.** Afterwards, rename the section to a sensible name (e.g. H_04) by right-clicking on the section in the Model Browser and choosing **Rename Section**. Delete the old (small) sections, but ensure that only the sections get deleted, but not their contents: Click on the section's name and push the "Delete" button of your keyboard. A window pops up, where **Delete Section only** is to select. In the new (big) section, you are now able to connect adjacent lines of the same horizon.

Open the Section View, select two lines you want to connect and select **Model Building → Data Modification → Join**. Smooth the line using the **Edit** tool.

Select all lines and click **Model Building → Data Modification → Resample**. Select resampling **Along Length** and a **Sample Interval** of 50 meters and click **Apply**. To create reliable surfaces, the lines have to be cut into little pieces of which the end points match and create surfaces with a sensible shape. To do so, click **Model Building → Data Modification → Split**, select the sub-tool **Split Lines and Polygons** and use the mode **Split with Points**. Now click on the spot on your line where it shall get split.

To create a surface, select the corresponding lines and click **Model Building → Surfaces/Volumes → Surface**. The sub-tool **Create Surface From Lines** should already be selected automatically. Use the method **Linear**. You can define a name and a color for your surface, but they also can be adjusted later. Finally, click **Create Surface**.

9.1.4 Further procedures

To add a DEM to the model, click **File** and choose **Insert…**. From the file format list on the bottom right of the opened window, choose **GIS Data – Raster Files** and navigate to the storage location of the DEM. Choose the file you want to import and click **Open**. A window pops up, where **As a grid where the data values represent elevation** has to be selected, then click **Next**. In the next two windows, nothing has to be changes, just click **Next**. The DEM has to be in the same projection system that already has been used for the images.

For the rotation to match the created surfaces to the DEMs, the following steps have to been taken. Delete all sections, because objects that belong to a section cannot get rotated, as well as the images. Ensure that the objects you want to rotate and the DEMs are visible. Select everything you want to rotate (usually horizons and surfaces) and click **Model Building → Data Modification → Transform**. From the list of **Transformation Types**, choose **Rotate (3 Axis)**. For **Center of Rotation**, choose **Selection**. Adjust the **Rotation Angle** of **X Axis** and **Y Axis** to the correct values or adjust the colored rotation circles that are displayed in the view window. If the result of the preview is satisfying, click **Transform** to perform the rotation.

In order to create a cross section through your finished model, open the **2D Map View**. Select **Model Building → Section Creation → Trace**. Choose a color, look and thickness for the section trace and select **No Snap** as **Creation Mode**. Choose the height where the section trace should be located. Click on the 2D Map to choose the starting and end points of your section trace. If desired, even more than two points are possible, creating a kinked section trace. Right-click to finish the creation of the section. A window pops up, where you can enter the name of the new section. After pressing **OK**,

the new section gets opened in Section View. Ensure that all surfaces of your model are visible in 3D or 2D view, as well as the DEMs. Then right-click on the new section's name in the Model Browser and choose **Collect All Intersections (Active View)**.

9.2 Overview of the images used

This table contains the following information about the radar images used for the creation of the 3D model.

- Section: The name of the section used MOVE, within the file petermann_horizons.mve
- Frame no.: The number of the data frame within CReSIS RDS data system
- Quality: This cells contain information about the reliability of the lines picked in this section, in order to create horizons gray_bottom and triple_mid. **1** = high, **2** = intermediate, **3** = low quality. The reliability types and their color code in the model are explained in chapter 4.3.2 – Picking prominent layers.
- Geographic coordinates: The longitude and latitude of the top left (TL) and bottom right (BR) edge of the image, possibly after cutting them.
- Bamber projection: LONG-LAT-values converted to the used Bamber projection.
- Parts cut: If only a part of the original image was used, here is remarked which parts were not used. For more explanation, see chapter 4.2 – Handling of images and data.
- Notes: If the flight route of an image was not entirely straight, this is remarked here.

The table is ordered by the name of the sections.

SECTION	FRAME NO.	QUALITY		GEOGRAPHIC COORDINATES			BAMBER PROJECTION			PARTS CUT	NOTES
		gray_bottom	triple_mid		LONG	LAT		x	y		
H06-1	20110507_01_011	1	1	TL	-58.224338	79.622827	TL	927771.73	-1017433.83	1st	
				BR	-56.82358	79.773768	BR	959035.827	-1010479.38		
H06-2	20110507_01_012	1,2	1,2,3	TL	-56.909151	79.764869	TL	957152.77	-1010896.1		
				BR	-54.608092	79.992612	BR	1006732.33	-999794.31		
H06-3	20110507_01_013	1,2	1,2,3	TL	-54.697243	79.984213	TL	1004850.51	-1000221.73		
				BR	-52.244781	80.200645	BR	1055486.94	-988833.976		
H06-4	20110507_01_014	1	1,3	TL	-52.337767	80.192934	TL	1053606.68	-989256.76	5th	
				BR	-51.02749	80.297805	BR	1079826.42	-983396.972		
H07-1	20110507_01_018	1	1	TL	-56.615887	79.713567	TL	960887.391	-1017990.83	5th	
				BR	-58.044864	79.560141	BR	928877.014	-1025084		
H07-2	20110507_01_017	1,2	1,2,3	TL	-54.41972	79.930748	TL	1008384.89	-1007280.51		
				BR	-56.700839	79.704603	BR	959005.828	-1018421.93		
H07-3	20110507_01_016	1,2	1,2,3	TL	-52.049522	80.139449	TL	1057516.63	-996184.578		
				BR	-54.508328	79.922378	BR	1006505.18	-1007711.1		
H07-4	20110507_01_015	1	1	TL	-50.870276	80.236661	TL	1081286.75	-990543.826	1st	
				BR	-52.142664	80.131848	BR	1055627.11	-996598.99		
H08-1	20110507_01_019	1	1	TL	-57.817245	79.511842	TL	931444.614	-1031557.17	1st	not quite straight
				BR	-56.404899	79.653758	BR	962863.47	-1025481.71		
H08-2	20110507_01_020	1,2	1,2,3	TL	-56.490449	79.645033	TL	960970.854	-1025888.41		
				BR	-54.179681	79.873868	BR	1011186.51	-1014502.14		
H08-3	20110507_01_021	1,2	1,2	TL	-54.267604	79.865489	TL	1009311.78	-1014942.58		
				BR	-51.84832	80.079211	BR	1059726.06	-1003456.63		
H08-4	20110507_01_022	1	1	TL	-51.940678	80.071618	TL	1057842.17	-1003877.81	5th	
				BR	-50.57017	80.182348	BR	1085547.99	-997497.16		
H09-1	20110507_01_026	1	1	TL	-56.179675	79.595254	TL	965201.277	-1032919.69	5th	not quite straight
				BR	-57.625083	79.437451	BR	932471.623	-1040509		
H09-2	20110507_01_025	1,2	1,2,3	TL	-53.986385	79.812387	TL	1013038.91	-1021972.2		
				BR	-56.264705	79.58659	BR	963312.926	-1033327.74		
H09-3	20110507_01_024	1	1	TL	-51.682906	80.015835	TL	1061245.56	-1010912.73		
				BR	-54.074968	79.804163	BR	1011147.75	-1022396.65		
H09-4	20110507_01_023	1	1	TL	-50.393612	80.119334	TL	1087414.71	-1004912.55	1st	
				BR	-51.773478	80.008178	BR	1059383.5	-1011351.3		
H10-1	20110507_01_027	1	1	TL	-57.321954	79.386854	TL	936503.775	-1047699.97	1st	not quite straight
				BR	-55.984303	79.534232	BR	966943.604	-1040446.78		
H10-2	20110507_01_028	1,2	1,3	TL	-56.068158	79.52535	TL	965062.509	-1040888.15		
				BR	-53.769516	79.753412	BR	1015452.38	-1029294.28		
H10-3	20110507_01_029	1,2	1,2	TL	-53.857316	79.745177	TL	1013567.61	-1029728.49		
				BR	-51.508127	79.953189	BR	1062997.92	-1018330.17		
H10-4	20110507_01_030	1	1	TL	-51.599321	79.945622	TL	1061117.15	-1018759.92	5th	
				BR	-50.100347	80.065334	BR	1091679.23	-1011785.81		
H11-1	20110507_01_034	1	1	TL	-55.777173	79.474188	TL	968989.464	-1047940.49	5th	
				BR	-57.127857	79.328174	BR	938224.205	-1055034.78		
H11-2	20110507_01_033	1,2	1,2,3	TL	-53.568039	79.692913	TL	1017583.18	-1036699.6		
				BR	-55.860365	79.465318	BR	967113.828	-1048388.55		
H11-3	20110507_01_032	1,2	1,2,3	TL	-51.329086	79.890917	TL	1064881.94	-1025724.83		
				BR	-53.655098	79.684726	BR	1015705.49	-1037136.55		
H11-4	20110507_01_031	1	1	TL	-50.036202	79.997963	TL	1091456.58	-1019255.46	1st	not quite straight
				BR	-51.41891	79.883062	BR	1063010.87	-1026194.67		

SECTION	FRAME NO.	QUALITY gray_bottom	triple_mid	GEOGRAPHIC COORDINATES		LONG	LAT	BAMBER PROJECTION		x	y	PARTS CUT	NOTES
H12-1	20110507_01_035	1	1	TL		-56.802646	79.281454	TL		942937.121	-1061944.22	1st	
				BR		-55.570508	79.414292	BR		971080.655	-1055415.96		
H12-2	20110507_01_036	1,2	1,2,3	TL		-55.653729	79.40545	TL		969197.813	-1055865.04		
				BR		-53.378149	79.631435	BR		1019514.53	-1044150.95		
H12-3	20110507_01_037	1,2	1,2,3	TL		-53.465062	79.623332	TL		1017633.46	-1044583.46		
				BR		-51.128379	79.830662	BR		1067265.74	-1032990.92		
H12-4	20110507_01_038	1	1	TL		-51.218206	79.823085	TL		1065392.58	-1033435.44	5th	not quite
				BR		-49.704981	79.943094	BR		1096525.71	-1026344.35		straight
H13-1	20110507_02_004	1	1	TL		-55.374599	79.353026	TL		972970.092	-1062973.77	5th	
				BR		-56.672566	79.212361	BR		943164.149	-1069965.66		
H13-2	20110507_02_003	1,2	1,2,3	TL		-53.177323	79.570903	TL		1021727.67	-1051554.66		
				BR		-55.457443	79.344275	BR		971089.569	-1063419.22		
H13-3	20110507_02_002	1,2	1,2,3	TL		-50.999097	79.764176	TL		1068196.68	-1040633.38		
				BR		-53.263615	79.562828	BR		1019851.06	-1051991.44		
H13-4	20110507_02_001	1	1	TL		-49.82277	79.860149	TL		1092608.48	-1034841.97	1st	
				BR		-51.08864	79.756674	BR		1066320.48	-1041072.96		
H14-1	20110429_01_009	1	1	TL		-57.149778	79.075171	TL		929165.028	-1081241.93		
				BR		-55.167683	79.293337	BR		975170.593	-1070428.6		
H14-2	20110429_01_010	1	1,2,3	TL		-55.249655	79.284575	TL		973299.308	-1070884.42		
				BR		-53.025301	79.506117	BR		1022931.72	-1059173.37		
H14-3	20110429_01_011	1,2	1,2,3	TL		-53.111423	79.497967	TL		1021047.18	-1059621.4		
				BR		-50.776362	79.706021	BR		1071138.64	-1047759.84		
H14-4	20110429_01_012	1	1	TL		-50.865635	79.698425	TL		1069257.47	-1048215.9	4th, 5th	
				BR		-49.28805	79.826115	BR		1102076.35	-1040396.2		
H15-1	20110429_01_016	1	1	TL		-54.94975	79.234596	TL		977665.953	-1077844.69	4th, 5th	
				BR		-56.247134	79.094145	BR		947648.617	-1084957.36		
H15-2	20110429_01_015	1	1	TL		-52.802279	79.447742	TL		1025725.75	-1066453.02		
				BR		-55.031361	79.225858	BR		975795.373	-1078304.69		
H15-3	20110429_01_014	1,2	1,3	TL		-50.59462	79.643623	TL		1073248.57	-1055173.65		
				BR		-52.887318	79.439465	BR		1023851.38	-1066924.89		
H15-4	20110429_01_013	1	1	TL		-49.192736	79.757841	TL		1102567.78	-1048080.92	1st, 2nd	
				BR		-50.684037	79.636257	BR		1071360.74	-1055608.36		
H16-1	20110429_01_017	1	1	TL		-56.428963	78.99107	TL		940664.509	-1094612.98	1st	
				BR		-54.719719	79.17736	BR		980497.294	-1085167.22		
H16-2	20110429_01_018	1	1,3	TL		-54.801689	79.168838	TL		978619.285	-1085607.59		
				BR		-52.621964	79.385694	BR		1027639.85	-1073916.63		
H16-3	20110429_01_019	1,2	1,2,3	TL		-52.70724	79.377602	TL		1025757.3	-1074371.27		
				BR		-50.410922	79.582296	BR		1075464.32	-1062478.37		
H16-4	20110429_01_020	1	1	TL		-50.49951	79.574826	TL		1073581.43	-1062931.57	4th, 5th	
				BR		-49.018246	79.694834	BR		1104712.65	-1055470.86		
H17-1	20110429_01_024	1	1	TL		-54.531132	79.115506	TL		982420.275	-1092743.98	4th, 5th	
				BR		-55.903231	78.967674	BR		950436.463	-1100315.86		
H17-2	20110429_01_023	1	1	TL		-52.418102	79.325491	TL		1030109.96	-1081294.23		
				BR		-54.612814	79.107058	BR		980542.287	-1093181.81		
H17-3	20110429_01_022	1,2	1,3	TL		-50.222143	79.519956	TL		1077802.17	-1069909.34		
				BR		-52.501906	79.317224	BR		1028244.08	-1081778.99		
H17-4	20110429_01_021	1	1	TL		-48.442535	79.668095	TL		1115349.79	-1060265.6	1st	not quite
				BR		-50.310912	79.512836	BR		1075914.39	-1070328.45		straight

SECTION	FRAME NO.	QUALITY gray_bottom	triple_mid	GEOGRAPHIC COORDINATES LONG	LAT	BAMBER PROJECTION x	y	PARTS CUT	NOTES
H18-1	20110429_01_025	1	1	TL -56.082462	78.865302	TL 943542.925	-1109945.06	1st	
				BR -54.316758	79.056965	BR 985003.193	-1100112.65		
H18-2	20110429_01_026	1	1	TL -54.398213	79.048452	TL 983120.68	-1100563.28		
				BR -52.223101	79.264971	BR 1032444.97	-1088661.46		
H18-3	20110429_01_027	1,2	1	TL -52.30707	79.25692	TL 1030573.46	-1089126.62		
				BR -50.027916	79.460231	BR 1080348.43	-1077077.28		
H18-4	20110429_01_028	1	1	TL -50.115579	79.452815	TL 1078467.63	-1077537.01	4th, 5th	
				BR -49.186777	79.529241	BR 1098254.58	-1072740.57		
V04-1	20100324_01_034	2,3	3	TL -56.455551	79.723966	TL 964218.928	-1017849.4		
				BR -58.499961	80.256261	BR 945785.956	-950271.767		
V04-2	20100324_01_033	1	1,3	TL -54.780036	79.236565	TL 981066.789	-1078586.89		
				BR -56.508914	79.738783	BR 963712.621	-1015988.99		
V05-1	20100324_01_030	2,3	3	TL -57.558998	80.17077	TL 959283.103	-964821.537	1st, 2nd	
				BR -56.150201	79.795679	BR 972229.957	-1012121.03		
V05-2	20100324_01_031	1	1,3	TL -56.204033	79.810549	TL 971713.714	-1010257.44		
				BR -54.482059	79.304945	BR 988940.527	-1073009.62		
V06-1	20100324_01_024	2,3	1,3	TL -55.632937	79.808635	TL 982237.988	-1013677.69	4th, 5th	
				BR -57.114037	80.20856	BR 968460.047	-963506.859		
V06-2	20100324_01_023	1	1,2,3	TL -54.005735	79.321566	TL 998758.727	-1073797.78		
				BR -55.686008	79.823629	BR 981724.211	-1011810.47		
V07-1	20100324_01_020	2,3	3	TL -57.323729	80.41828	TL 971966.17	-940506.431		
				BR -55.336476	79.884065	BR 990068.637	-1007383.27		
V07-2	20100324_01_021	1,2	1,2,3	TL -55.389166	79.899112	TL 989561.149	-1005517.57		
				BR -53.715318	79.397597	BR 1006574.69	-1067253.75		
V08-1	20100324_01_018	2,3	3	TL -54.800006	79.891659	TL 1000208.88	-1009438.92		
				BR -56.82483	80.440048	BR 981332.122	-941058.42		
V08-2	20100324_01_017	1,2,3	1,3	TL -53.452896	79.48373	TL 1014049.8	-1059449.28	1st	
				BR -54.851715	79.906704	BR 999702.727	-1007583.63		
V09-1	20100324_01_014	2,3	1	TL -56.052995	80.398338	TL 993373.278	-949623.011	1st	
				BR -54.486772	79.963872	BR 1008115.9	-1003444.43		
V09-2	20100324_01_015	1,2	1,3	TL -54.538813	79.978959	TL 1007601.58	-1001587.89		
				BR -52.792768	79.441784	BR 1025755.48	-1067132.37		
V10-1	20100324_01_012	2,3	3	TL -53.986655	79.981994	TL 1017835.03	-1004035.96		
				BR -55.948024	80.524497	BR 999227.674	-936983.337		
V10-2	20100324_01_011	1,2	2,3	TL -52.287833	79.449701	TL 1035810.37	-1068661.78		
				BR -54.03784	79.99715	BR 1017323.92	-1002181.41		
V11-1	20110507_02_017	1	2,3	TL -55.459599	80.555153	TL 1008602.12	-936296.075		
				BR -53.950107	80.137139	BR 1022887.7	-987811.218		
V11-2	20110507_02_018	1,2	1,2,3	TL -54.002206	80.152408	TL 1022376.65	-985944.911		
				BR -52.651859	79.742154	BR 1036267.82	-1035837.03		
V11-3	20110507_02_019	1,2	1,3	TL -52.700433	79.757569	TL 1035747.12	-1033973.27		
				BR -51.530916	79.370509	BR 1048729.04	-1080522.88		
V11-4	20110507_02_020	1	1	TL -51.575782	79.386033	TL 1048214.15	-1078665.87	5th	
				BR -50.884884	79.14214	BR 1056338.35	-1107771.15		
V12-1	20110429_02_006	1	1,2	TL -54.199075	80.376886	TL 1025257.72	-961284.102	1st, 2nd	
				BR -53.644427	80.214499	BR 1030568.57	-981084.927		
V12-2	20110429_02_007	1	1,2	TL -53.697688	80.229693	TL 1030032.01	-979225.965		
				BR -52.250218	79.787232	BR 1045017.16	-1032854.94		

SECTION	FRAME NO.	QUALITY gray_bottom	triple_mid		GEOGRAPHIC COORDINATES LONG	LAT		BAMBER PROJECTION x	y	PARTS CUT	NOTES
V12-3	20110429_02_008	1,2	1,2,3	TL	-52.29845	79.802619	TL	1044493.2	-1031000.46		
				BR	-51.087585	79.396724	BR	1058085.39	-1079625		
V12-4	20110429_02_009	1	1	TL	-51.13248	79.41235	TL	1057560.11	-1077761.52	5th	
				BR	-50.317939	79.119388	BR	1067316.93	-1112570.52		
V13-1	20110429_02_005	1	1,2	TL	-53.192917	80.249195	TL	1039632.94	-979495.754	4th, 5th	
				BR	-53.770281	80.416684	BR	1033943.54	-959102.32		
V13-2	20110429_02_004	1	1,2	TL	-51.809681	79.819413	TL	1054131.64	-1031347.86		
				BR	-53.245603	80.264476	BR	1039097.8	-977635.417		
V13-3	20110429_02_003	1	1,3	TL	-50.655022	79.42634	TL	1067275.9	-1078241.68		
				BR	-51.856216	79.835016	BR	1053633.55	-1029482.44		
V13-4	20110429_02_002	2	1	TL	-49.744012	79.095205	TL	1078479.68	-1117446.93	1st	
				BR	-50.697972	79.442169	BR	1066781.78	-1076368.95		
V14-1	20110429_01_033	1	1,2	TL	-52.56115	80.243681	TL	1050858.72	-982890.503	1st	not quite straight
				BR	-51.412043	79.86875	BR	1062803.1	-1027753.19		
V14-2	20110429_01_034	1	1	TL	-51.460131	79.884219	TL	1062264	-1025900.22		
				BR	-50.159612	79.434793	BR	1077219.08	-1079303.27		
V14-3	20110429_02_001	1	1	TL	-50.138231	79.427253	TL	1077480.96	-1080196.73	4th, 5th	
				BR	-49.515989	79.195347	BR	1085130.61	-1107528.67		
V15-1	20110429_01_032	1	1,2	TL	-51.005989	79.912085	TL	1071433.78	-1024767.08	5th	
				BR	-52.179891	80.286872	BR	1058814.72	-979924.47		
V15-2	20110429_01_031	1	1	TL	-49.860421	79.513975	TL	1084753.37	-1071933.16		
				BR	-51.051904	79.92774	BR	1070930.38	-1022907.68		
V15-3	20110429_01_030	1	1	TL	-48.995931	79.197664	TL	1095689.96	-1109181.22	1st	
				BR	-49.904651	79.529727	BR	1084213.74	-1070072.52		